University of Alberta

TEST PARTICLE SIMULATIONS OF GLOBAL TRANSPORT IN EARTH'S
MAGNETOSPHERE

by

Ding Li

A thesis submitted to the Faculty of Graduate Studies and Research in partial
fulfillment of the requirements for the degree of **Master of Science**

Department of Physics

Edmonton, Alberta

Spring, 2006

Library and
Archives Canada

Bibliothèque et
Archives Canada

Published Heritage
Branch

Direction du
Patrimoine de l'édition

395 Wellington Street
Ottawa ON K1A 0N4
Canada

395, rue Wellington
Ottawa ON K1A 0N4
Canada

NOTICE:
The author has granted a non-exclusive license allowing Library and Archives Canada to reproduce, publish, archive, preserve, conserve, communicate to the public by telecommunication or on the Internet, loan, distribute and sell theses worldwide, for commercial or non-commercial purposes, in microform, paper, electronic and/or any other formats.

AVIS:
L'auteur a accordé une licence non exclusive permettant à la Bibliothèque et Archives Canada de reproduire, publier, archiver, sauvegarder, conserver, transmettre au public par télécommunication ou par l'Internet, prêter, distribuer et vendre des thèses partout dans le monde, à des fins commerciales ou autres, sur support microforme, papier, électronique et/ou autres formats.

The author retains copyright ownership and moral rights in this thesis. Neither the thesis nor substantial extracts from it may be printed or otherwise reproduced without the author's permission.

L'auteur conserve la propriété du droit d'auteur et des droits moraux qui protège cette thèse. Ni la thèse ni des extraits substantiels de celle-ci ne doivent être imprimés ou autrement reproduits sans son autorisation.

In compliance with the Canadian Privacy Act some supporting forms may have been removed from this thesis.

Conformément à la loi canadienne sur la protection de la vie privée, quelques formulaires secondaires ont été enlevés de cette thèse.

While these forms may be included in the document page count, their removal does not represent any loss of content from the thesis.

Bien que ces formulaires aient inclus dans la pagination, il n'y aura aucun contenu manquant.

Canada

Abstract

Two case studies of large scale particle transport, using a test particle approach in Earth's magnetosphere, are presented. The first case considers different possible entry paths of solar wind plasma into the magnetosphere for quiet geomagnetic conditions. Solar wind plasma is captured in the high latitude cusp region and subsequently enters the magnetosphere. Most of the penetrating particles flow into the tail. Nevertheless, some particles drift into the inner magnetosphere and populate the boundary layers and plasma sheet. Other particles are trapped around Earth and produce a ring current-like region. The second case considered focuses on electron response to a transient process triggered by solar wind dynamic pressure pulse. The results illustrate electron adiabatic injections and corresponding energy flux enhancements, and suggest that the induced earthward $\mathbf{E} \times \mathbf{B}$ drift has an effect on particle transport and energization during the dipolarization-like process associated with solar wind pressure pulse.

Acknowledgement

This thesis is the result of two years of work in the Department of Physics, at the University of Alberta. where I have been encouraged and supported by many people. With a deep-felt gratitude, I wish to express my sincere thanks to both of my supervisors. Dr. Richard Marchand and Dr. Robert Rankin, for their constructive comments and motivating discussions during the development of this thesis. Under their guidance, I learned the way of scientific research and began my computational study of space physics. Their timely encouragements helped build the confidence and enthusiasm needed for scientific research, and helped me stay focused through my project, which are greatly appreciated.

I also want to thank, Dr. Konstantin Kabin, who provided the necessary background fields from his global MHD simulations, and for taking the time to have many helpful discussions. Thanks to Dr. Ian Mann, Dr. Martyn Unsworth and other members in the space physics group. who gave me many critical suggestions when I presented my research in the committee meetings and seminars.

Finally, I am grateful for the technical support from Academic Information and Communication Technologies at the University of Alberta, and from WestGrid.

Contents

List of Tables

List of Figures

List of Abbreviations

- **IMF** Interplanetary Magnetic Field

- **MHD** Magnetohydrodynamic

- **LLBL** Low Latitude Boundary Layer

- **KHI** Kelvin Helmholtz Instability

- **GSM** Geocentric Solar Magnetic

Chapter 1

Introduction

1.1 Interaction of the Solar Wind with the Earth's Magnetosphere

1.1.1 Solar wind and interplanetary magnetic field

The solar wind is a supersonic flow of plasma which is continuously ejected from the outermost region of the Sun (corona) into interplanetary space. The mechanism of continuous solar wind formation was first explained by Parker, assuming an equilibrium state model [Park, 1958]. He showed that the thermal energy of solar corona plasma (about 200eV) is high enough to be able to escape gravitational attraction and form a constant streaming outflow.

Because of the high electrical conductivity of solar wind plasma, magnetic field lines are frozen in the plasma, in the sense that magnetic field lines must move outward with the expanding solar wind, thus forming what is called the interplanetary magnetic field (IMF). The solar wind moves out almost radially from the corona in the Sun's frame of reference. The rotation of the Sun, however, gives the magnetic field a spiral form.

1
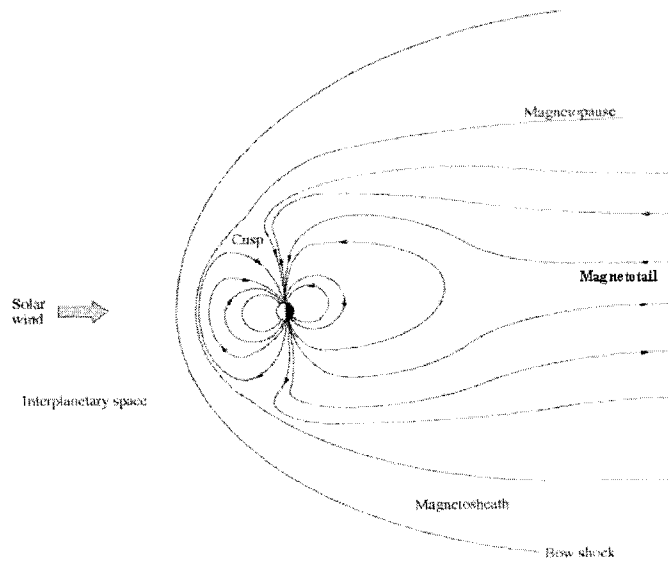
Figure 1.1: Illustration of the main components of the Earth's magnetosphere, from
http://www.physics.arizona.edu/physics/news/matters/fall96/spacephy.html

1.1.2 Basic configuration of Earth's magnetosphere

The magnetosphere is the plasma environment in space around Earth extend-
ing to approximately ten Earth radii ($R_E = 6370$km) in the dayside, to several
hundreds R_E away in the nightside, which shape is controlled by the interaction
of Earth's magnetic field and the IMF. Because the solar wind is supersonic,
there is a shock boundary, in front of the Earth's magnetosphere, called the
bow shock. The outer boundary of the magnetosphere is called the magne-
topause, and the magnetosheath is the region between the bow shock and the
magnetopause (See Figure 1.1). The plasma in the magnetosheath originally
comes from the solar wind. Its density is typically larger than the solar wind
density and the inner magnetospheric plasma density.

The magnetosphere is pulled out on the nightside and forms the long tail-
like region called the magnetotail. A schematic cross section of the magnetotail
is illustrated in Figure 1.2. The region close to the magnetopause is defined
as the boundary layer. It can be divided into a plasma mantle and a low

2
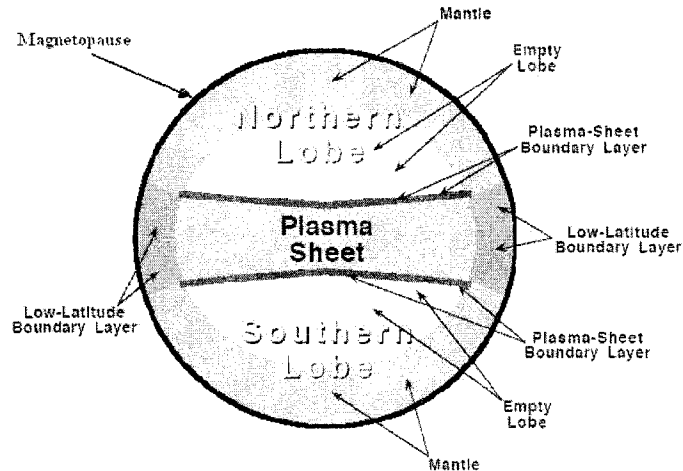
Figure 1.2: Cross section of the magnetotail showing the principal plasma regions, from Joe Borovsky, http://www-ssc.igpp.ucla.edu/gem/tutorial/2004/borovsky.pdf

latitude boundary layer (LLBL). The layer of tailward moving plasma inside the high latitude magnetosphere is identified as plasma mantle, and the LLBL is the layer near the equator. The detailed configurations of these regions are affected by the direction of IMF: the LLBL is thicker for northward IMF while the plasma mantle is thicker for southward IMF [Sckopke and et al., 1981]. The plasma sheet is the region of closed field lines located in the centre of the magnetotail near the equatorial plane. A typical particle density there is about $0.5 cm^{-3}$. The average particle energies are 0.6 keV for the electrons and 5.0 keV for the protons. The low density regions between plasma sheet and plasma mantle are called lobes, in which the magnetic field lines are open and nearly parallel or anti-parallel to the sun-Earth line. In addition, there is a transit region observed between the plasma sheet and plasma lobes named the plasma sheet boundary layer (PSBL).

1.1.3 Magnetic reconnection

Magnetic reconnection is a fundamental physical phenomenon occurring in a magnetized plasma. It changes the topology of magnetic fields by break-

3
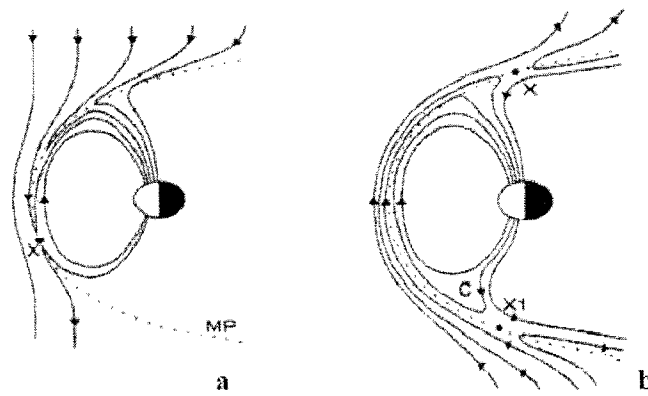
Figure 1.3: A schematic illustration of magnetic reconnection with different IMF (from [Lockwood, 1995])

ing magnetic lines and reconnecting them in a different way. The concept of magnetic reconnection was first applied to magnetospheric physics by Dungey [1961]. When the oppositely pointing IMF and geomagnetic field lines approach each other, the open geomagnetic field lines, with one end on Earth and the other in interplanetary space, are formed by reconnection and establish a link between the Earth's field and the IMF. Dungey was primarily concerned with southward IMF, which results in a first reconnection in the subsolar region at the magnetopause and a second one in the X-point at the distant tail. For northward IMF, reconnection occurs at the tailward cusp region, where the orientation of Earth's magnetic field lines and IMF are also antiparallel. Figure 1.3 shows the dayside magnetic reconnections with different IMF conditions (1.3a represents the southward IMF situation, 1.3b represents the northward IMF situation), where X-point is the place of reconnections occurrence [Lockwood, 1995]. Through solar wind-Earth interaction, magnetic reconnection provides a natural mechanism for mass, momentum, and energy transport from the solar wind into the magnetosphere, and it drives large scale magnetospheric convection.

4

1.2 Transport Processes in the Magnetosphere

1.2.1 Contribution of different plasma sources to the magnetosphere

The two main sources of plasma in the magnetosphere are the solar wind, as an external source, and the ionosphere, as an internal source. In order to understand some open questions concerning entry and transport mechanisms, and assess the relative origins of plasma in the magnetosphere, it is necessary to consider a combination of simulation studies and observations. Usually the solar wind source dominates the distant region from Earth and the ionospheric source dominates the near-Earth region. The exact relative contribution, however, depends on the solar wind conditions and other geomagnetic conditions.

1.2.2 Possible entry and transport mechanisms for solar wind plasma

Several mechanisms have been proposed to account for the transport of the solar wind plasma into the magnetosphere. Two of the principal ones are described below.

Magnetic reconnection: The dayside reconnection model refers to the merging of the geomagnetic and interplanetary magnetic fields somewhere on the magnetopause. The reconnection also connects the magnetosheath flux tubes with the magnetospheric flux tubes as they are pulled along into the magnetotail by the solar wind. The reconnecting field lines lead to an open access for solar wind plasma across the magnetopause through plasma flow. In previous studies [Raeder and et al., 1997, Song et al., 1999], it is noted that most of the plasma flow simply passes around the magnetosphere along the open field lines, without going through the inner magnetosphere and plasma sheet.

5

Kelvin-Helmholtz instability: The Kelvin-Helmholtz instability (KHI) is not a direct mass transport process. However, when the KHI occurs under various sharp shear boundary conditions, it develops large scale flow patterns (KHI vortices) along the boundary layers, which distort the magnetopause surface and lead to magnetosheath particle trapping and mass transport across the magnetopause and boundary layers [Fujimoto and Terasawa, 1994]. Although plasma entry along the tail flank induced by KHI has been observed and simulated [Fujimoto and et al., 1998], the question of whether this process contributes on the dayside magnetopause or at the inner edge of the LLBL is still an open question.

There are some other entry mechanisms, but they are of lesser importance. In test particle code simulations discussed in this thesis, only the effect from magnetic reconnection will be considered.

1.2.3 Transport during a transient process in the near-Earth region

During certain transient processes of the magnetosphere, the local magnetic field configuration may change rapidly. This, in turn, is usually associated with strong induced electric fields. As a consequence, particles in the inner magnetosphere are accelerated and redistributed. In particular, during the expansion phase of a substorm, the magnetic field in the nightside may rapidly relax to a more dipolar-like configuration. This process is referred to as dipolarization. Dipolarizations are generally accompanied by sudden increasing fluxes of energetic particles around the Earth (accounting for particle injections), as observed by geostationary satellites [Cummings et al., 1968, Walker et al., 1976]. These injections sometimes appear simultaneously at all energies. For that reason, the phenomenon is also called dispersionless injection, and it is regarded as one of the well-known features of magnetospheric substorm onsets. Re-

6

cently, however, there are observations of nonstorm time flux enhancements, characteristic of the dispersionless injection, which are associated with the solar wind pressure pulse [Lee and Lyons, 2004, Lee et al., 2004].

1.3 Simulations of Plasma Transport Process in the Magnetosphere

Test particle models offer a convenient method for studying the source, transport and loss processes in the solar-terrestrial environment. They require the prescription of a magnetic and electric field configuration, which should describe the global state of the magnetosphere and magnetotail.

Compared with full particle codes, test particle models are not self-consistent because they don't include the feedback from particle motion to current systems. Test particle models, however, allow us to trace the paths of particles and provide the dynamic evolution through the entire region modelled by the global MHD models, while the full particle codes are typically limited to electron scale and tend to be restricted to small simulation regions.

Over the past decade, several test particle models used the forward calculation to trace particle trajectories from a given source, for the purpose of determining the mechanisms of entry and transport, and understanding how the various regions of the magnetosphere are populated. For example, Ashour-Abdalla et al., [1993] use a full Lorentz particle trajectory calculation in empirical electric and magnetic fields to study the magnetotail formation and boundary layer structure from a plasma mantle source. Using a similar technique, Delcourt et al., [1994] investigate the population of the plasma sheet from the ionospheric source. Alternatively, several authors calculate particle trajectories using more realistic magnetosphere configurations from the global MHD models (such as the UCLA model, Ogino model) and the asso-

7

ciated self-consistent electric fields [Richard et al., 1994, Walker et al., 1996, Peroomian, 2003]. In their simulations, they consider the transport of particles from solar wind sources under different IMF conditions. For example, Richard et al., [1994] study particle transport with northward IMF; Walker et al., [1996], on the other hand, focus on southward IMF; while Peroomian [2003] considers continuously changing IMF conditions. All of their results confirm that magnetic reconnection is the predominant mechanism for solar wind particle entry: for northward IMF, solar wind particles enter mostly from the high latitude reconnection region while for southward IMF their entrance is around the sub-solar reconnection region. It should be noted that test particle codes generally don't include diffusion or wave particle interaction associated with KHI. Only a small number of test particle simulations coupled with global MHD models (UCLA model, [Ashour-Abdalla et al., 1997]) have been made to track individual test particles from a measured distribution function backward in time, and determine the locations and strengths of the sources.

One difficulty with full Lorentz particle codes is that they require considerable computing times. A numerically, more efficient alternative is to consider particle trajectories in the guiding centre approximation. Some test particle codes have applied the guiding centre approximation with simple analytic field models [Li et al., 1998, Li et al., 2003] and global MHD models (LFM MHD model, [Elkington et al., 2002], Birn's model, [Birn et al., 1998]) to simulate particle dynamics and transport processes in the near-Earth regions during storm time.

This thesis is motivated by previous successes of test particle simulations, and by recent observations of (1) the dense plasma sheet during northward IMF and (2) the energetic electron injections associated with nonstorm event. Using a modern global MHD model (BATS-R-US, [Powell et al., 1999]),

we re-examine the contribution of the solar wind with northward IMF, to the formation of a dense plasma sheet and inner magnetospheric boundaries (Chapter 3), and simulate the injection of energetic electrons during a transient dipolarization-like event associated with the solar wind pressure decrease (Chapter 4).

9

Chapter 2

Guiding centre theory and numerical approach

2.1 Single Particle Motion

Plasma is a gas composed of charged particles. The fundamental equation describing the motion of a particle with charge q and mass m in a magnetic field $\mathbf{B}$ and electric field $\mathbf{E}$ is the Lorentz equation

$$\frac{d\mathbf{p}}{dt} = q(\mathbf{E} + \mathbf{v} \times \mathbf{B}), \tag{2.1}$$

where $\mathbf{v}$ is the particle's velocity. The momentum $\mathbf{p}$, considering special relativity, is given by

$$\mathbf{p} = \gamma m \mathbf{v}, \tag{2.2}$$

where the Lorentz factor is

$$\gamma = (1 - \frac{v^2}{c^2})^{-\frac{1}{2}}. \tag{2.3}$$

Equation 2.1 can be solved analytically in some simplified magnetic and electric fields. The basic motion of charged particles in a magnetized plasma is to

10
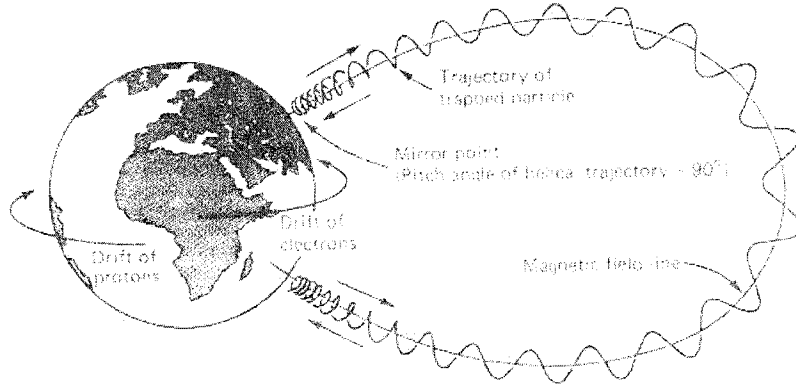
Figure 2.1: Trajectory of trapped electrons and protons experiencing magnetic mirroring, gradient and curvature drifts in the geomagnetic field

gyrate around the magnetic field line. The gyroradius of a particle is given by

$$\rho = \frac{\gamma m v_\perp}{qB},$$
(2.4)

where $v_\perp$ is the component of particle's velocity perpendicular to the local magnetic field. The period of the gyration motion, called the gyroperiod, is given by

$$T = \frac{2\pi \gamma m}{|q|B}.$$
(2.5)

The pitch angle is defined as the angle between the particle velocity and the magnetic field and is given by

$$\alpha = \arctan(\frac{v_\perp}{v_\parallel}),$$
(2.6)

where $v_\parallel$ is the component of particle's velocity parallel to the local magnetic field.

There are three main characteristic drifts: the $\mathbf{E} \times \mathbf{B}$ drift, the grad-$\mathbf{B}$ drift and the curvature drift [Northrop, 1963]. In the Earth's magnetic field, particles perform a slow longitudinal drift around the Earth. Electrons drift

11

eastward while ions drift westward (see Figure 2.1).

2.2 First Adiabatic Invariant

If the magnetic field varies slowly enough over space and time compared with gyroradius and gyroperiod, that is, if

$$\varepsilon_r = max\{|\frac{\rho\nabla_\perp B}{B}|, |\rho\nabla_\parallel \hat{b}|\} \ll 1 \tag{2.7}$$

and

$$\varepsilon_t = |\frac{T}{B}\frac{\partial B}{\partial t}| \ll 1, \tag{2.8}$$

where $\hat{b}$ is the unit vector along the local magnetic field, the ratio of perpendicular component of kinetic energy $W_\perp$ to the magnitude of the magnetic field B is approximately invariant. This approximate constant of the motion is the first adiabatic invariant (also called magnetic moment), and it is defined as

$$\mu = \frac{W_\perp}{B} = \frac{\gamma m v_\perp^2}{2B} = \frac{\gamma m v^2 \sin^2 \alpha}{2B}. \tag{2.9}$$

In a slowly varying magnetic field without parallel electric field $E_\parallel$ (parallel to the magnetic field), where the first adiabatic invariant and particle's kinetic energy are conserved, Equation 2.9 implies that the pitch angle has to increase as the magnetic field strength increases. When the pitch angle reaches 90° at the mirror points, $v_\parallel$ vanishes and the particle is reflected back along the field line. The bounce motion between mirror points is described by the mirror force equation as

$$F_\parallel = -\frac{1}{2}qv_\perp\rho\nabla_\parallel B = -\frac{\mu}{\gamma}\hat{b}\cdot\nabla B, \tag{2.10}$$

12

where the force is parallel to the magnetic field and tends to reflect a particle out of a region with high magnetic field.

2.3 Guiding Centre Theory

When the adiabatic conditions (Equations 2.7 and 2.8) are satisfied, a charged particle's motion can be described as gyration superposed on the drift motion of the guiding centre. This guiding centre motion consists of the drift velocity perpendicular to **B** plus the velocity component along **B**.

$$\frac{d\vec{r}}{dt} = \vec{v_d} + \vec{v_\parallel},\tag{2.11}$$

$$\vec{v_d} = \frac{\vec{E} \times \hat{b}}{B} + \frac{\mu}{qB\gamma}\hat{b} \times \nabla B + \frac{\gamma m v_\parallel^2}{qB}(\nabla \times \hat{b})_\perp,\tag{2.12}$$

$$\frac{dp_\parallel}{dt} = qE_\parallel + \frac{p_\parallel}{B}\vec{E} \cdot (\nabla \times \hat{b})_\perp - \frac{\mu p_\parallel}{qB\gamma}(\nabla \times \hat{b})_\perp \cdot \nabla B - \frac{\mu}{\gamma}\hat{b} \cdot \nabla B.\tag{2.13}$$

where $\vec{v_d}$ is the particle's drift velocity and $p_\parallel$ is the component of particle's momentum parallel to the local magnetic field. The three terms on the right hand side of Equation 2.12 represent respectively the **E**×**B** drift, the grad-**B** drift and the curvature drift. In all terms, both **B** and **E** are evaluated at the guiding centre position.

In the Lorentz equation, the particle's motion is described by six coupled first-order equations in a three dimensional coordinate system: three equations for the velocity and three equations for the acceleration. Using the guiding centre approximation, the description of particle motion reduces to four equations: three equations for velocity and one for the parallel acceleration.

13

2.4 Numerical Approach to Simulate Particle Motion

In addition to the background fields, the essential information required to solve particle motion are the position and parallel momentum. From the input initial conditions, including the particle's initial position $\vec{r}$, energy W_0, pitch angle α and species (m,q), the initial parameters are calculated as

$$\mu = \frac{W_0}{B(\vec{r},0)}(1 + \frac{W_0}{2mc^2})\sin^2\alpha, \tag{2.14}$$

$$\gamma_0 = 1 + \frac{W_0}{mc^2}, \tag{2.15}$$

$$P_{\|0} = [(\frac{W_0}{c})^2 + 2mW_0]\cos\alpha, \tag{2.16}$$

where $B(\vec{r},0)$ is the magnitude of magnetic field calculated at the initial position, γ_0 and $P_{\|0}$ are the initial Lorentz factor and parallel momentum. Since the first adiabatic invariant μ is conserved in the guiding centre approximation, this quantity only needs to be calculated from the initial conditions. Two essential relations used through the calculations are shown as follows,

$$\gamma = \frac{1}{mc}(m^2c^2 + 2m\mu B(\vec{r},t) + p_\|^2)^{\frac{1}{2}} \tag{2.17}$$

and

$$v_\| = \frac{p_\|}{m\gamma}. \tag{2.18}$$

Combined with the Equations 2.11, 2.12 and 2.13, these are self-consistent equations that describe particle motion in the guiding centre approximation. The most common numerical approach used to solve these coupled ordinary differential equations is the fourth-order Runge-Kutta method, and the time

14
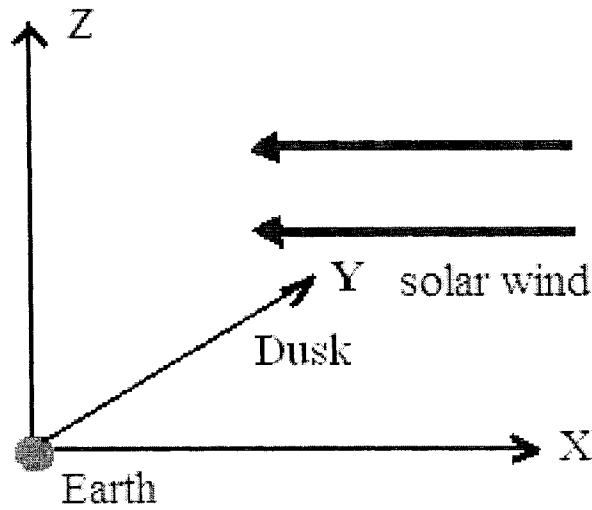
Figure 2.2: Illustration of the GSM coordinate system

step is usually around one tenth of the particle's gyroperiod.

The geocentric solar magnetic (GSM) coordinate system is used in this thesis (see Figure 2.2). The x-axis is defined along the line connecting the centre of the Earth to the centre of the Sun, and is positive towards the Sun. The y-axis is oriented along the cross product of the GSM x-axis and the magnetic dipole axis and directed positive towards dusk. The z-axis is defined as the cross product of the x- and y-axes. By construction, the magnetic dipole axis lies within the XZ plane.

According to the guiding centre theory, a charged particle in the static magnetic fields is predicted to undergo both bounce and drift motions. In order to test the validity of the test particle code in the guiding centre approximation, a proton is traced for half drift period in a magnetic dipole field, with energy 1MeV and an initial pitch angle of $30°$, by using both the guiding centre equations and the full Lorentz equations. The simulation times for the guiding centre approach and the full Lorentz approach are 0.01 second and 1.32 seconds respectively. The guiding centre approach is numerically faster because it uses

15
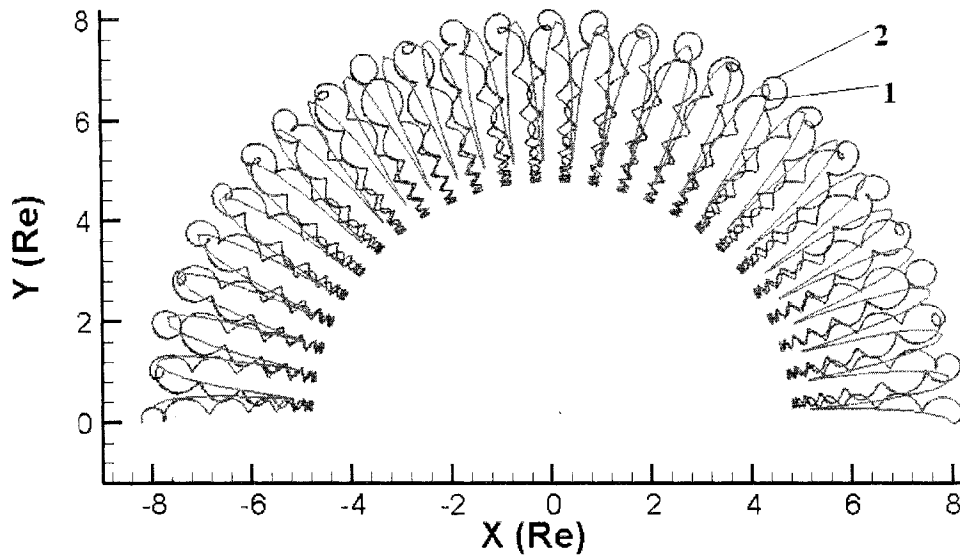
Figure 2.3: Projection in the XY plane of calculated trajectory of trapped protons using both guiding centre equations (label 1) and full Lorentz equations of motion (label 2) in a dipole field. In both cases, the proton is located initially at x=$8R_e$, y=0, with initial energy 1MeV and a pitch angle of 30°.

a larger time step and it requires solving fewer equations than the full Lorentz approach.

As illustrated in Figure 2.3, the proton's motion includes periodic bouncing and drift due to the varying field (gradient and curvature drifts), as expected. The trajectory obtained in the guiding centre approximation (label 1), however, does not exactly match the actual trajectory (label 2), obtained with the full Lorentz integration. Compared with the full Lorentz trajectory, the guiding centre trajectory has noticeable differences in the bounce period and the positions of the mirror points. The pitch of the azimuthal drifts are also seen to differ slightly between the two methods of calculation.

In this calculation, the bounce periods obtained in the guiding centre approach and in the full Lorentz approach are $T_{gc} = 13.57$ seconds and $T_{full} = 14.85$ seconds respectively. The relative difference between these two periods is $\Delta T/T_{full} = 0.086$. When the calculation is repeated with a lower

16

energy $W_0 = 100\text{KeV}$, other initial conditions being the same, the relative difference between the two bounce periods is $\Delta T / T_{full} = 0.067$ ($T_{gc} = 44.32$ seconds, $T_{full} = 47.52$ seconds). The agreement between the guiding centre approach and the full Lorentz approach is therefore seen to be better for lower energy particle, as expected.

Another quantitative difference between the two approaches is that, in the guiding centre approximation, the particle bounces 14 times while drifting azimuthally by 180 degrees while, with the full Lorentz calculation, the same azimuthal drift requires 13 bounces. These numbers change to 43 and 42 respectively for a particle with energy 100keV, other initial conditions being the same. This illustrates that results obtained in the drift approximation will generally be quantitatively different from the ones obtained with a more accurate full Lorentz integration technique. The drift approximation, however, is deemed adequate to study large scale properties of the system under consideration.

The exact invariance of the magnetic moment μ follows an asymptotic series in the order of ϵ [Northrop, 1963],

$$\mu = \mu_0 + \epsilon \mu_1 + \epsilon^2 \mu_2 + \cdots, \tag{2.19}$$

where $\epsilon = \frac{\rho}{l}$ (ρ is the gyroradius and l is the characteristic length of the varying fields). The magnetic moment $\mu_0 = \frac{mv_\perp^2}{2B}$ is the lowest order approximation to the asymptotic expansion of the first adiabatic invariant [Northrop, 1963]. To investigate the oscillation amplitude of magnetic moment, let $\Delta \mu$ be the amplitude of the fluctuation in the magnetic moment normalized to μ_0.

17
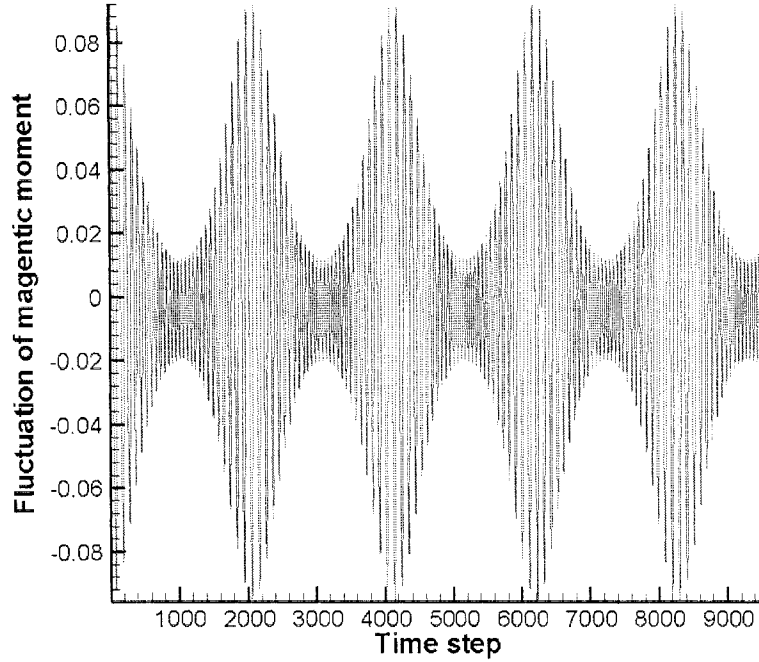
Figure 2.4: Variation in the magnetic moment calculated from a full Lorentz particle trajectory integration. The particle has the same initial conditions as in Figure 2.3.

$$\Delta\mu = \frac{\mu - \mu_0}{\mu_0} \propto \epsilon = \frac{\rho}{l}. \tag{2.20}$$

If a higher order expression of the magnetic moment were used here, the order of $\Delta\mu$ would be much smaller. The computation, however, becomes more complicated. For the guiding centre approximation, $\Delta\mu = 0$. Figure 2.4 shows the fluctuation of magnetic moment with the full Lorentz calculation. The magnetic moment oscillates about a constant value (μ_0) on a time scale of the order of gyroperiod and its magnitude varies on a time scale of the order of bounce period. The fluctuation is minimum when the particle is close to the mirror points and it is largest around the equatorial plane. The magnetic moment is nonetheless considered to be approximately conserved,

18

since its relative oscillations are small. We note that the relative variations in μ due to finite gyroradius effects, increase with particle energy. For a given field configuration, the validity of the drift approximation is therefore limited in particle energy and magnitude of the magnetic field. Specifically, particle gyroradii increase with increasing energy. At a particular position, the adiabatic condition stated in Equation 2.7 will therefore break down for particles above a certain energy. For the same reason, the guiding centre approach is more valid in regions with stronger magnetic fields.

2.5 Scaling Experiment for Parallel Computation

In this test particle code, millions of particle trajectories are traced in order to calculate the spatial density and other macroscopic plasma properties. It is therefore necessary to apply parallel computation to solve this relatively large problem.

Speedup is a useful criterion for evaluating the performance of parallel computation. It is defined as the ratio of execution time on a single processor to that on multiple processors.

$$S(n) = \frac{T_1}{T_n}, \tag{2.21}$$

where n is the number of processors, T_1 is the execution time on a single processor and T_n is the execution time on n processors.

It is expected that applying n processors to the parallel computation should cause it to complete n times faster, which is the ideal speedup. Unfortunately, most computer programs fail to scale linearly with the number of processors,

19

which has led to several empirical scaling laws for actual applications. For example, in *Amdahl's law*, if f is the fraction of operations in a problem which has to be done sequentially, the best possible speedup S(n) is bounded by

$$S(n) = \frac{n}{1 + (n-1)f} \rightarrow \frac{1}{f}, \text{as } n \rightarrow \infty.$$ (2.22)

Therefore, the actual speedup is always smaller than the ideal speedup and the maximum speedup is $\frac{1}{f}$, irrespective of n. If the code has a significant sequential component, large-scale parallelism may not be useful. However, considering more factors that affect the parallel performance, such as communications among CPUs and time delay for I/O, there should be obvious gaps between the actual speedup and Amdahl's speedup. Based on that, Minsky conjectured that the speedup increases approximately as the logarithm of the number of processors [Minsky and Papert, 1971].

In the test particle model considered here, the serial portion of the code includes reading input files and initialization. The other part for tracing particles are parallelized using OpenMP. A numerical experiment is made to assess scaling on the Cortex (IBM SMP machines) of WestGrid. The problem size is fixed, with 12000000 particles and 25 time steps. In order to avoid the poor concurrency among CPUs, particles are distributed evenly among all processors. The number of processors is varied from 2 to 32 in power of 2. The actual execution times with varying number of processors are used to construct the speedups shown in Table 2.1. This table also includes the speedups estimated from *Amdahl's law*, together with those corresponding to fit with Minsky's empirical formula. It should be mentioned that the same scaling experiment is repeated using more particles (48000000) and that similar results are found.

20

Table 2.1: Parallel performance: speedup and efficiency

nCPU	Amhadl's speedup	Minsky's speedup	Actual speedup
2	1.986	2	1.971
4	3.918	4	3.829
8	7.626	6	5.956
16	14.480	8	7.882
32	29.385	10	9.178
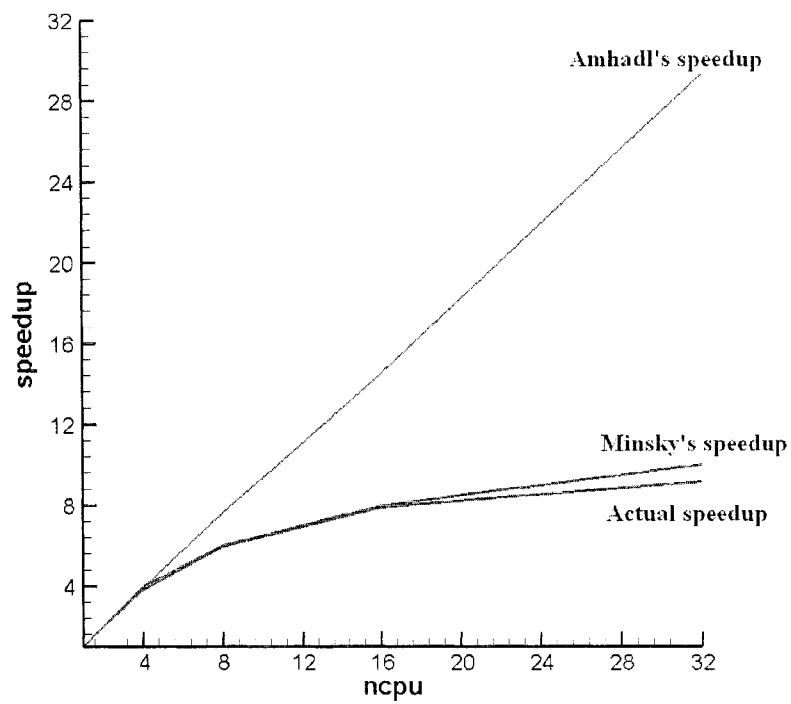
Figure 2.5: Relationship between different speedups and the number of processors

21

It is clear in Figure 2.5 that the difference between Amdahl's speedup and the actual speedup is widening with an increasing number of CPUs. Nevertheless, the observed speedup is consistent with the Minsky speedup, increasing proportionally to the logarithm of the number of processors. The breakdown of Amdahl's speedup results from the external overhead which are ignored in *Amdahl's law.* From the results of this simple scaling experiment, it follows that relatively modest speedup can be expected for this test particle model using OpenMP. This suggests that another approach to parallel computation, perhaps MPI, might be preferable for such calculations.

Chapter 3

Modelling large scale transport of the solar wind ions during northward IMF

3.1 Observations of the Cold Dense Plasma Sheet and Possible Source

It has been recognized that the plasma sheet becomes dense and cold during extended period of the northward IMF. Much evidence [Terasawa and et al., 1997, Øieroset et al., 2003, Hasegawa et al., 2004], obtained from in-situ satellite observations, has been presented and suggested that the magnetosheath plasma from solar wind is the major source for the cold dense plasma sheet during the northward IMF.

Using the Geotail data averaged over 9 hours prior to the plasma sheet observations, Terasawa et al., [1997] conclude that there is a positive correlation between the north-south angle of the IMF and the ion density of the near-Earth plasma sheet ($15R_E < X_{GSM} < 50R_E$). They also note that the density of the plasma sheet increases and the temperature decreases during dominantly northward IMF periods.

Another statistical study from the Wind satellite [Øieroset et al., 2003] covering the plasma sheet earthward of $X_{GSM} = -24R_E$, together with the

23
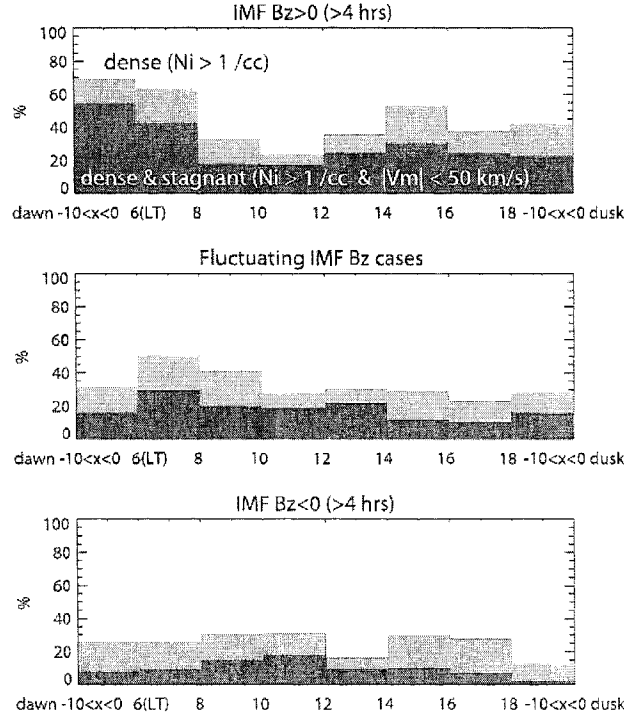
Figure 3.1: Occurrence probability of dense ion region (lightly shaded histogram) dependence on magnetic local time and IMF conditions (from Hesegawa et al., [2004])

Terasawa's Geotail study, confirm that the entire plasma sheet tailward of $X_{GSM} = -50R_E$ is cold and dense after a prolonged interval of northward IMF. All these observations point out that the dense ion region is located predominantly on the flanks. Figure 3.1 [Hasegawa et al., 2004] displays the dependence of the occurrence probability of a dense ion region, which is represented by the light shaded histogram, in the plasma sheet on the magnetic local time (MLT), and on the IMF condition. This result is from the analysis of 50 months of Geotail data. The magnetic local time before 8MLT and after 16MLT corresponds respectively to the dawn and dusk flanks for these observations. It is clear that the flank regions have a high probability of having a dense ion population in northward IMF.

The weak dawn-dusk asymmetry shown in Figure 3.1 has also been reported by Wing et al., [2002]. They average the plasma sheet ion density and

24
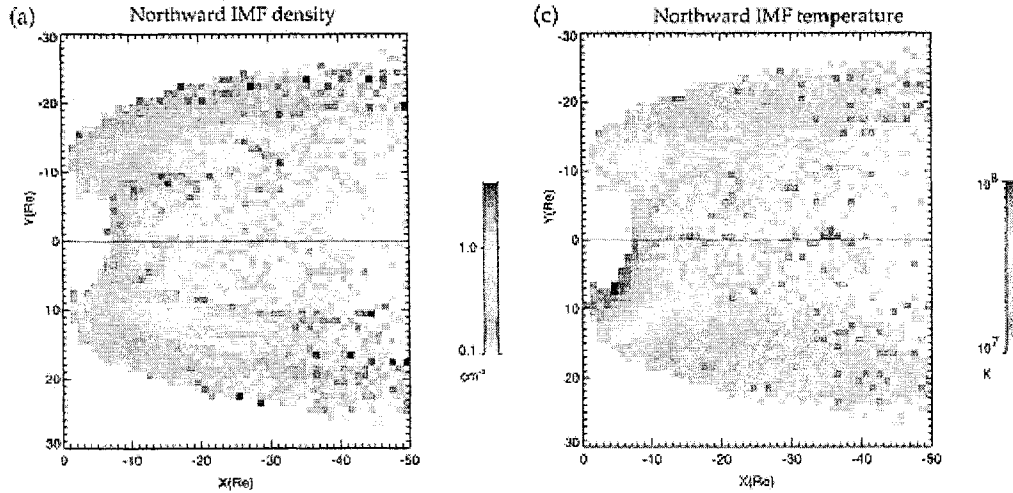
Figure 3.2: Ion density and temperature 2D profiles on the equatorial plane for northward IMF (from [Wing and Newell, 2002])

temperature from the DMSP ionospheric observations over longer time intervals [Wing and Newell, 2002], and map them into the 2D equatorial plane in the nightside as shown in Figure 3.2. This figure shows in detail that the ion density has a maximum along the plasma sheet flanks and that the dawn side is a little denser than the dusk side during northward IMF. The near-Earth region is also seen to be highly populated. However, the minimal ion temperature occurs near the flanks under the same conditions.

The observations discussed in this section strongly confirm that the cold dense plasma sheet occurs for periods of prolonged northward IMF. It is well known that the solar wind and ionospheric plasma are two dominating sources for the inner magnetosphere. Nevertheless, based on observed ion composition, the cold O^+, a characteristic component of ionospheric outflow, is absent in the cold dense plasma sheet [Fujimoto and et al., 1998]. Therefore, solar wind plasma is the primary source for the cold dense plasma sheet with northward IMF.

25

3.2 Modelling

3.2.1 Simulation method

Rather than attempting to include all possible physical mechanisms for the formation of cold dense plasma sheet during northward IMF, the approach followed here concentrates on the dynamic transport of the source charged particles from the solar wind using a test particle approach, which is more direct and simple for modelling large scale mass transport. In this model, a large number of non-interacting test particles are followed through the electric and magnetic fields obtained from a global MHD model. The MHD approximation offers a generally physically realistic description of the magnetosphere and its interaction with the solar wind, and some important effects such as reconnection and convection are also included in the MHD model. Furthermore, a realistic time-varying field configuration can be obtained from a global MHD simulation because it can be driven with the real-time parameters from satellites, including upstream solar wind and IMF conditions. The field configurations used in this thesis are obtained from the BATS-R-US global MHD model. For reference, the structure of the test particle code is illustrated in Figure 3.3.

Most observations of magnetospheric particle distributions are for ions because electrons have more possible origins and these origins are more difficult to discriminate. Therefore low energy ions are used mainly as tracers for defining different source regions of particles in the magnetosphere. When the adiabatic conditions are satisfied, the guiding centre approximation is used to track the particle trajectories, which allows large time steps and, thus, saves computation time.

As mentioned previously, the magnetic field used for particle tracing is obtained from a global MHD simulation. In the ideal MHD model, the resistive

26
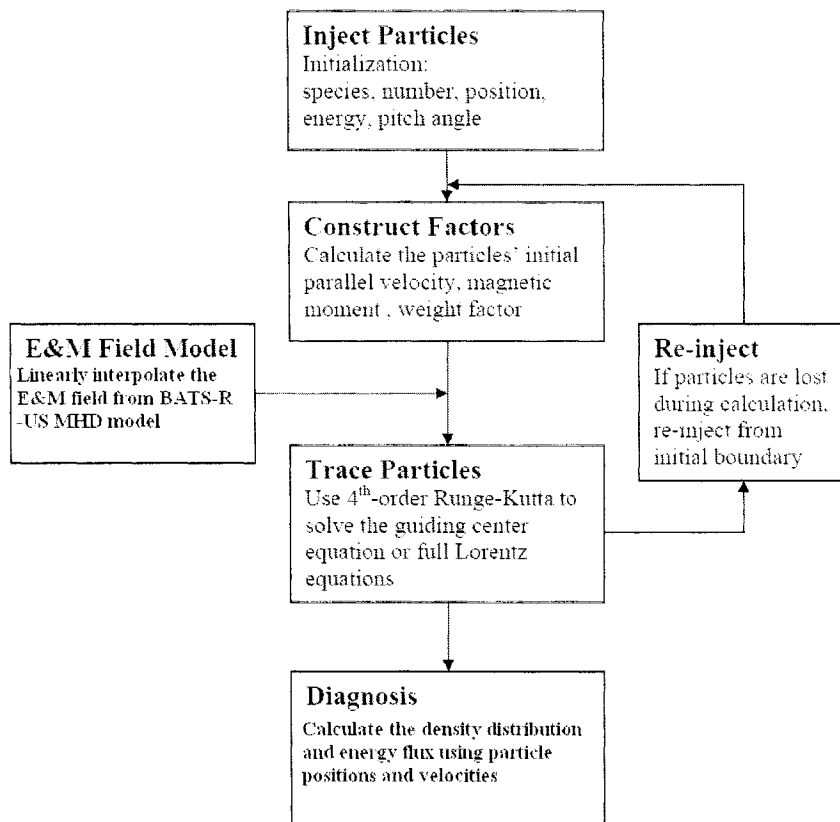
Figure 3.3: Logic diagram for the test particle code

27

term is zero and the electric fields can be calculated by using

$$\vec{E} = -\vec{V}_{MHD} \times \vec{B}, \tag{3.1}$$

where $\vec{V}_{MHD}$ is the bulk flow velocity and $\vec{B}$ is the magnetic field. Integrating particle trajectories requires the instantaneous fields, which are obtained by using multilinear interpolation in space between neighboring grid points. In order to avoid large interpolation errors near the Earth, the spatial interpolation of the field is calculated from reduced BATS-R-US fields, in which the dominant dipole field has been subtracted. The dipole component of the field is added analytically in the calculation of the trajectories, which uses the fourth order Runge-Kutta integration technique.

Idealized solar wind parameters and IMF condition are used as input for the BATS-R-US simulation code. In this case, the IMF is initially southward. It rapidly flips northward and remains constant thereafter. The time dependence of the dipole tilt is also taken into account. The simulation domain is the rectangular prism made of 101 by 81 by 81 nodes, which extends from $-80R_E$ to $20R_E$, $-40R_E$ to $40R_E$, and $-40R_E$ to $40R_E$ in the x, y, z axes (GSM coordinates) respectively. The grid size is $1R_E$ and a fixed time step of 1 second (around one tenth of the gyroperiod) is used throughout. Because the BATS-R-US code uses an unstructured mesh with adaptive mesh refinement, the fields data from BATS-R-US are interpolated to the regular mesh used in the test particle code. When the magnetosphere configuration approaches the quasi-steady state, 10,000,000 ions of thermal energy $10eV$ (in the drifting solar wind frame of reference) with Maxwellian distribution function are continuously injected across the plane $x = 19R_E$, upstream of the simulated bow shock. Each particle i carries a relative weight $W(i)$ determined at the

28

time of injection in order to account for the specified uniform flux of solar wind, $2.0 \times 10^{12} m^{-2} s^{-1}$. Particles are removed from the simulation box and re-injected from the $x = 19 R_E$ plane wherever one of the following conditions is met: 1. The test particles cross the outer boundaries of simulation box ($x = 20 R_E$, $x = -80 R_E$, $y = \pm 40 R_E$ and $z = \pm 40 R_E$); 2. The test particles cross the inner boundary ($R \leq 3 R_E$); 3. The test particles motion becomes non-adiabatic.

A large number of particle trajectories are traced and each particle's position and velocity are recorded at every time step. Particle number density and other quantities can be calculated from these values. To calculate the number density, the entire simulation space is divided into $101 \times 81 \times 81$ bins of $1 R_E^3$ volume. For a specific time, it is possible to determine which bin the particle (i) is passing through. The contribution to density in the vertex (k) of this bin (j) by this particle (i) is given by

$$n_{ijk} = \frac{W(i) \times R(k)}{V_j},\tag{3.2}$$

where W(i) is the relative weight of particle (i), R(k) is the relative weight of vertex (k) and V_j is the volume of the cell ($1 R_E^3$).

In this case, the vertex relative weight R(k) is computed from its relative position to the particle in a given cell. The relative weight W(i), which represents each particle's contribution to the initial distribution, is assigned when the particle is injected, as

$$W(i) = \frac{n_s \times v_s \times A \times \Delta t}{N(t)},\tag{3.3}$$

29

where n_s and v_s are the solar wind density and flow velocity, A is the source boundary area and $N(t)$ is the total number of injected particles at time t and Δt is the time step. In this simulation, $n_s = 5cm^{-3}$, $v_s = 400km/s$, $A = 80 * 80R_E^2$, Δt=1s and N(0)=10,000,000.

The density contribution of vertex k from cell j is determined from the contribution of all the particles contained in that cell:

$$n_{jk} = \sum_i n_{ijk}. \qquad (3.4)$$

Since every vertex k may belong to more than one cell, the total number density at vertex k is the summation over all these adjacent cells:

$$n_k = \sum_j n_{jk}. \qquad (3.5)$$

3.2.2 Entry trajectories of solar wind ions

To start with, the main features of the background fields obtained from the global MHD simulation are considered. Figure 3.4 shows the configuration of a steady state magnetosphere with northward IMF. Here an empirical formula for the location and shape of the magnetopause is used to visualize the boundary [Petrinec and Russell, 1996]. This empirical shape depends on the distance downtail (x), solar wind momentum flux (ρv_{sw}^2) and the north(south)ward component of IMF (b_n or b_s):

Table 3.1: MHD and Particle Tracing Model Parameters

Solar wind density (amu/cm^3)	5
Solar wind velocity (km/s)	400
Interplanetary magnetic field (nT)	5
Particle initial distance (R_E)	19
Particle initial kinetic energy (eV)	10
Tracing time step (s)	1

$$
\begin{aligned}
R_{tail} = {} & \sqrt{((\varepsilon^2 - 1)x^2 - 2\varepsilon(1 + \varepsilon)r_0 x)\Theta(x) + r_0^2(1 + \varepsilon)^2} \\
& + [\frac{-2}{0.085}\arcsin\sqrt{2.98(\rho\nu_{sw}^2)^{-0.524}e^{0.085x}(0.152 - \{{}^{0.00137b_n}_{0.00644b_s}\})} \\
& - \arcsin\sqrt{2.98(\rho\nu_{sw}^2)^{-0.524}(0.152 - \{{}^{0.00137b_n}_{0.00644b_s}\})}]\Theta(-x). \quad (3.6)
\end{aligned}
$$

where R_{tail} is the distance from Earth to the magnetopause in unit of R_E, Θ is the Heaviside step function, $r_0 = (10.30 \pm 0.18 + (0.16 \pm 0.03) \times b_s) \times (\rho\nu_{sw}^2/2.1)^{-\frac{1}{6}}$, and $\varepsilon = -1 + (14.63 \pm 0.50)/(10.30 \pm 0.18 + (0.16 \pm 0.03) \times b_s)$. The parameters of this magnetopause location model were obtained empirically from observations. In this calculation, the values for the solar wind dynamic pressure ($\rho\nu_{sw}^2 = 1.33nPa$) and IMF ($b_n = 5nT$) are taken to be the same as in the MHD simulation (other model parameters are listed in Table 3.1). Although the analytic formula is an approximation for the location of the magnetopause, it matches well with the MHD simulation result when comparing the predicted magnetopause surface (thick blue line) with the visual magnetopause boundary from the simulated solar wind density contour distribution in the noon-midnight plane (Figure 3.4). Also all the closed magnetic fields are inside this predicted magnetopause on the dayside. Therefore, the empirical formula does seem to provide an acceptable approximation for the purpose of determining solar wind particles penetrating the magnetosphere.

31
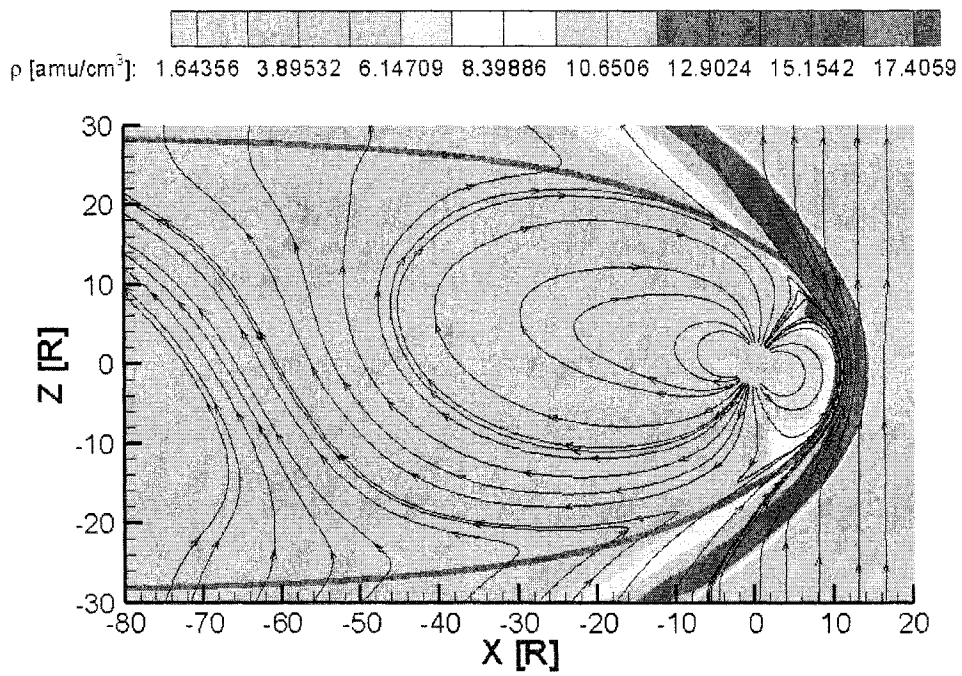
Figure 3.4: Magnetic field configuration and density contour in the noon-midnight plane, from BATS-R-US MHD simulation with northward IMF. The blue line shows the location of Petrinec and Russell's empirical magnetopause.

Further examining the magnetic field configuration in Figure 3.4, it appears that the high latitude reconnection between the IMF and the magnetospheric field occurs in the polar cusp region of both hemispheres. The reconnection process connects the magnetosheath flux tubes with the magnetospheric flux tubes, which has been suggested as a source of mass, energy and momentum transfer from solar wind to the magnetosphere [Richard et al., 1994, Song et al., 1994, Song et al., 1999, Richard et al., 2002]. In addition, the new closed field lines are formed on the dayside during the reconnection process [Song et al., 1999, Watanabe et al., 2005] while the closed field lines on the nightside are extended to the mid-tail region. For the open magnetic field lines, only a few are with one foot connected to the Earth. Therefore, the magnetosphere in the northward IMF is nearly closed [Song et al., 1999].

Among the three kinds of drift motions of trapped particles, the $\mathbf{E} \times \mathbf{B}$ drift velocity is dominant in most magnetospheric regions of interest here. In this study, the electric field is obtained from the ideal MHD simulation (see Equation 3.1), specifically

$$
\begin{aligned}
\vec{V}_{E \times B} &= \frac{\vec{E} \times \vec{B}}{B^2} = \frac{-(\vec{V}_{MHD} \times \vec{B}) \times \vec{B}}{B^2} \\
&= \frac{(\vec{B} \cdot \vec{B})\vec{V}_{MHD} - (\vec{B} \cdot \vec{V}_{MHD})\vec{B}}{B^2} = \vec{V}_{MHD} - V_{\parallel}\hat{b},
\end{aligned}
\tag{3.7}
$$

where $V_{\parallel}$ is the component of flow velocity parallel to the local magnetic field.

Figure 3.5 shows the streamlines with the density contour background in the noon-midnight and equatorial planes. The streamlines are along the bulk flow velocity. Outside the bow shock, they are perpendicular to the interplanetary magnetic field ($V_{\parallel} = 0$). From Equation 3.7, the solar wind plasma undergoes $\mathbf{E} \times \mathbf{B}$ drift in the same direction as the bulk flow, towards the bow shock. A large number of the streamlines are diverted around the boundary

33

ρ [amu/cm^3]: 1.64356 3.89532 6.14709 8.39886 10.6506 12.9024 15.1542 17.4059

a

30

20

10

Z [R] 0

-10

-20

-30
-80 -70 -60 -50 -40 -30 -20 -10 0 10 20
X [R]

b

30

20

10

Y [R] 0

-10

-20

-30
-80 -70 -60 -50 -40 -30 -20 -10 0 10 20
X [R]
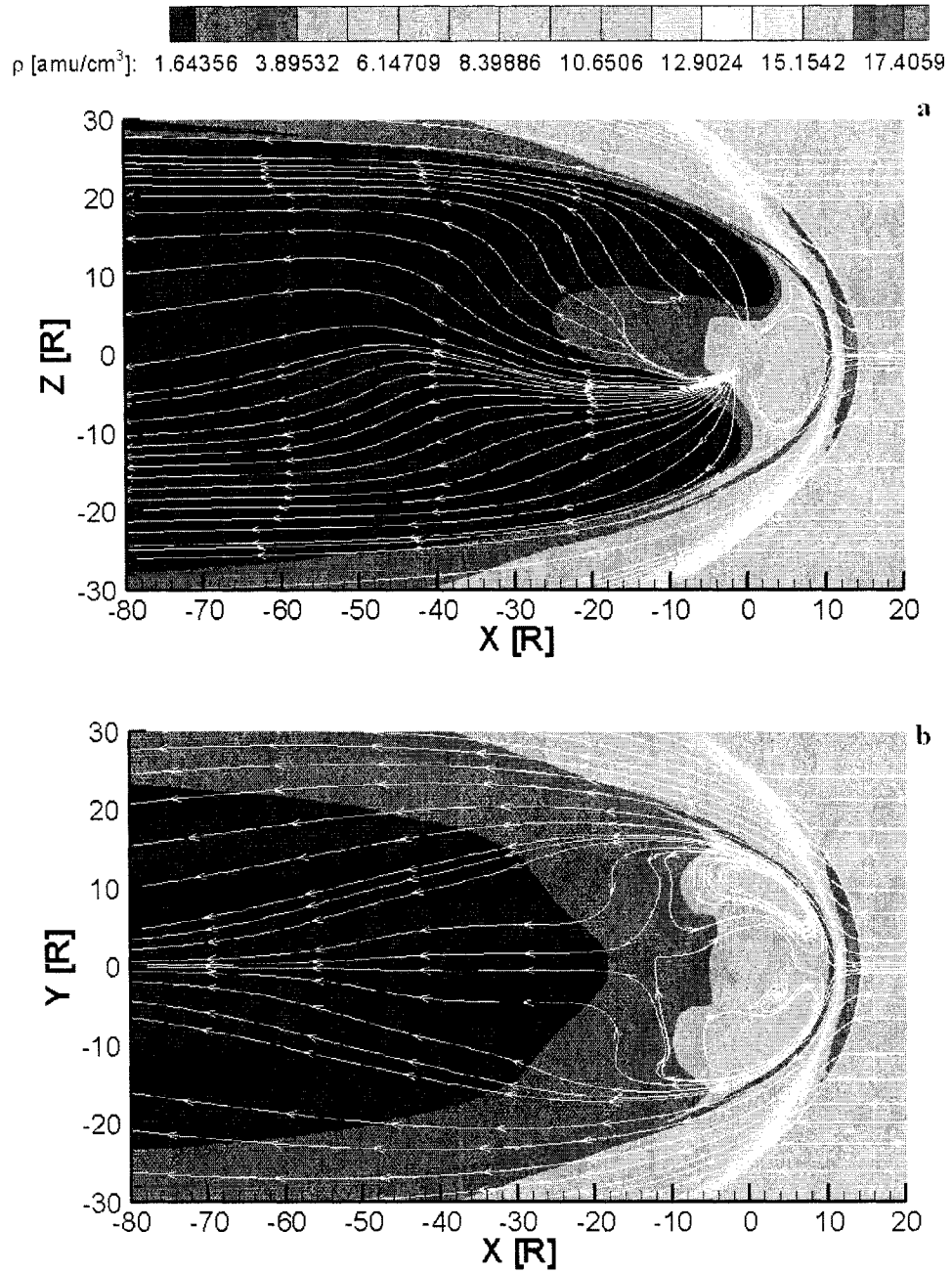
Figure 3.5: Flow velocity fields and density contours in the noon-midnight (a) and equatorial planes (b) from BATS-R-US MHD simulation with northward IMF

34
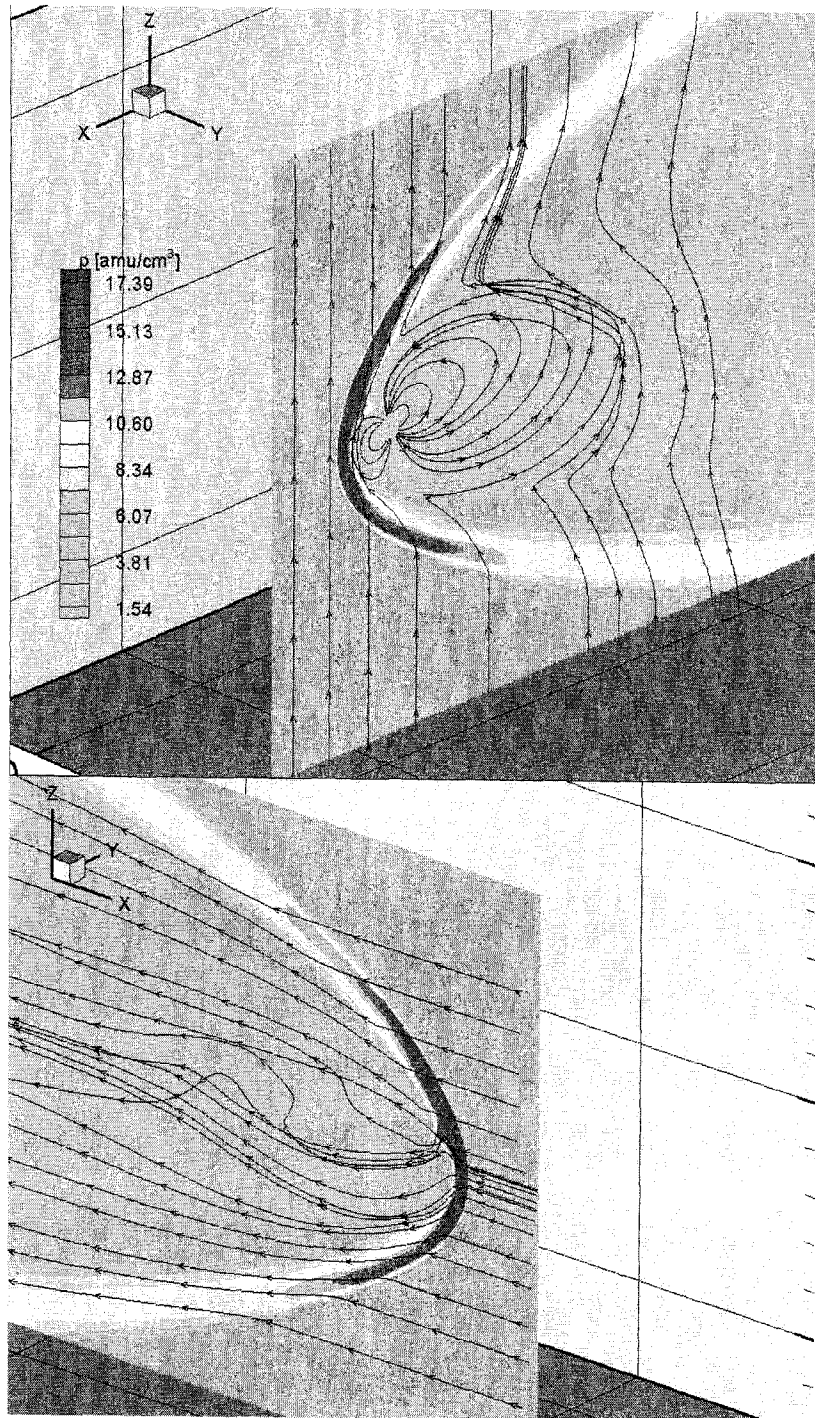
Figure 3.6: Magnetic field lines and bulk streamlines in 3D with density contours in the noon-midnight plane from BATS-R-US MHD simulation with northward IMF. The top panel illustrates the magnetic field lines viewed from the dusk side. The bottom panel shows the streamlines viewed from the dawn side.

35

layer after crossing the bow shock. However, some streamlines come into the magnetosphere from the high latitude reconnection region (Figure 3.5a). The entering streamlines then move along the boundary layers into the tail, while some of them move around the flank into the near-Earth tail and produce the closed cells in the equatorial plane (Figure 3.5b). The three dimensional perspective of magnetic field lines and streamlines obtained from the global MHD simulation are shown in Figure 3.6.

In this study, 10,000,000 ions are injected upstream of the bow shock in the prescribed magnetic and electric fields. Many of the solar wind particles are reflected by the bow shock. However the magnetosheath is eventually populated by the solar wind plasma. The particles that cross the bow shock are heated and their magnetic moment may not be conserved exactly. Nevertheless, the intent of this study is to investigate the mass transfer from the magnetosheath particles, which come from the solar wind, into the inner magnetosphere. For this purpose, the variation of magnetic moment at the bow shock can be neglected and the guiding centre approximation is adequate to describe the large scale mass transport. The configuration of bulk streamlines suggests that solar wind plasma mostly flows into the tail around the magnetopause. This is confirmed by the simulation results, in which the majority of the ions do not enter the magnetosphere. For those particles penetrating the magnetosphere, a large fraction passes by the plasma mantle in the high latitude or low latitude boundary layer and flows antisunward into the tail region without becoming trapped (see Figure 3.7).

Some of the particles cross the magnetopause and become trapped in the vicinity of the Earth. This kind of trapping, however, is not permanent. If a particle stays long enough around the Earth, it is regarded as being trapped. An illustration of such trapped particle is shown in Figure 3.8. The trajectory

36
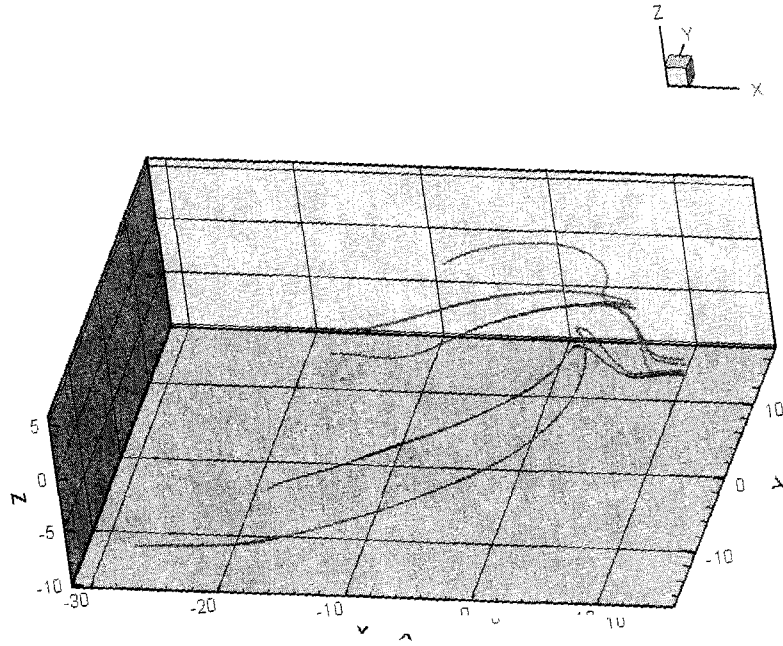
Figure 3.7: Example trajectories for solar wind particles flowing into the tail without being trapped

and the shape of the magnetopause are indicated in blue and black respectively. The top panel gives the equatorial perspective and the bottom panel shows the noon-midnight perspective. The ion first approaches the subsolar magnetopause through the $\mathbf{E} \times \mathbf{B}$ drift. When the newly closed magnetic field lines are formed on the dayside, the ion drifts to the high latitude and enters the magnetosphere from the cusp region, which can be identified from the background density contours. It then moves to the dawn side flank, eventually across the magnetotail and is trapped around the Earth because of the gradient and curvature drifts.

Figure 3.9 shows another ion trajectory in the same format as Figure 3.8. It is also clear that the ion enters the magnetosphere through the high latitude cusp region. However, it then bounces about the equator on the dawn side, bypasses the low latitude boundary layer flank, and drifts to the nightside. Subsequently it flows into the tail to form the plasma sheet without remaining

37
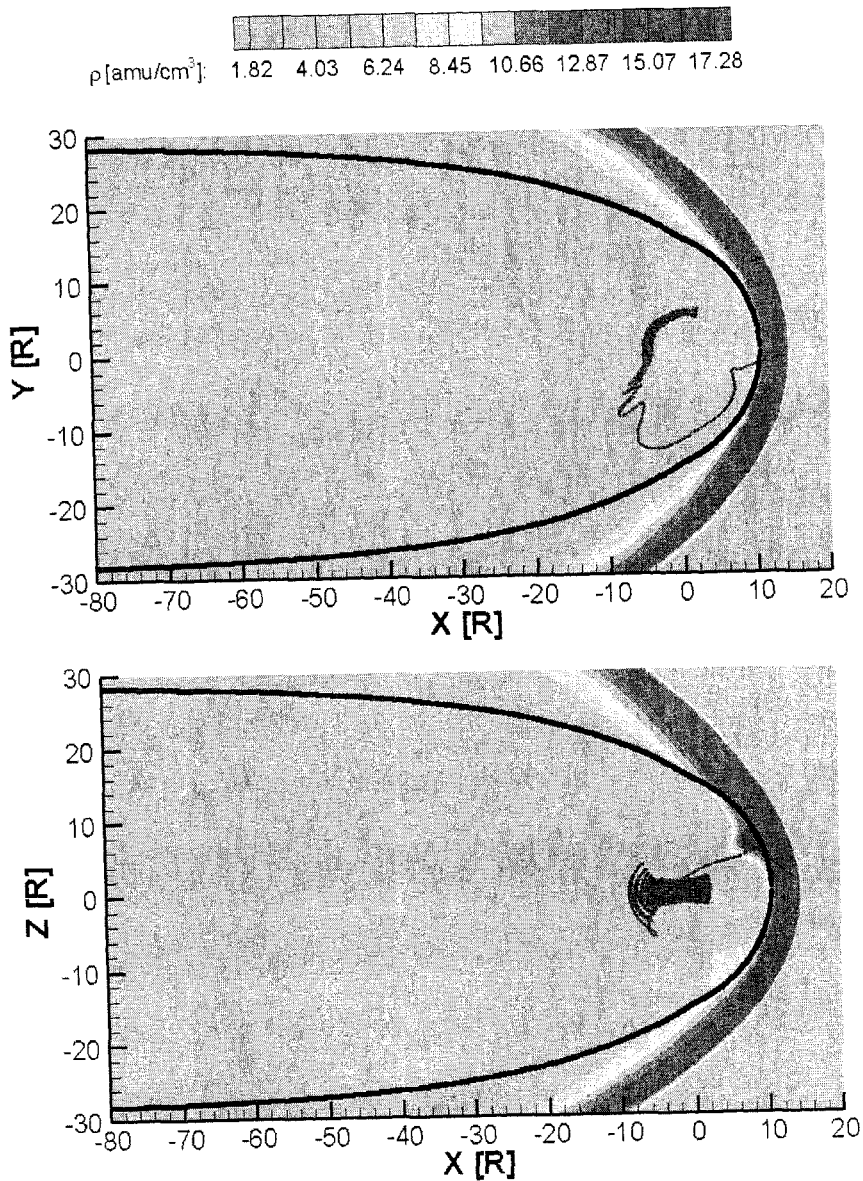
Figure 3.8: Example trajectory for solar wind particle entering into the magnetosphere and being trapped around the Earth. The background density profile is from BATS-R-US global MHD simulation. The top panel gives a equatorial perspective and the bottom panel shows a noon-midnight meridian perspective.

38
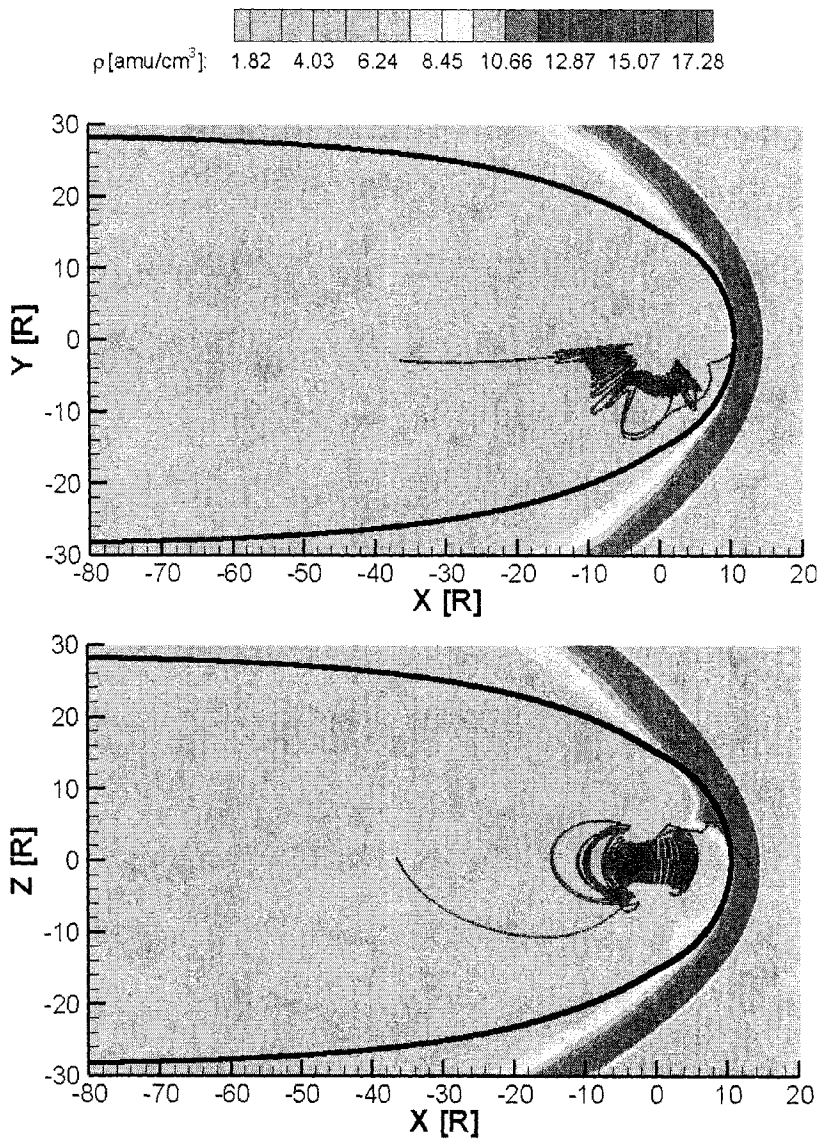
Figure 3.9: Example trajectory for solar wind particle entering into the magnetosphere and flowing along the dusk LLBL into the tail. The background density profile is from BATS-R-US MHD simulation. The top panel gives a equatorial perspective and the bottom panel presents a noon-midnight meridian perspective.

39
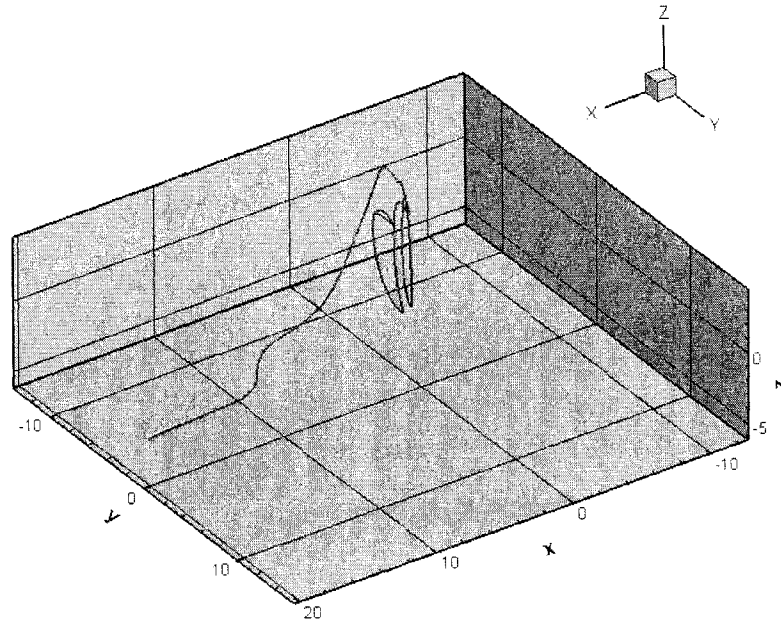
Figure 3.10: Example trajectory for a solar wind particle entering the magnetosphere along the low latitude boundary on the flanks, without transiting through the cusp

trapped. As it moves further from the Earth, the influence from the gradient and curvature drifts becomes smaller than the $\mathbf{E} \times \mathbf{B}$ drift. This is why the particle keeps moving antisunward into the tail and becomes untrapped.

Although the entry routes of the penetrating particles primarily pass by the high latitude reconnection region, some particles may enter the magnetosphere along the low latitude boundary on the flanks without transiting through the cusp (see Figure 3.10), which suggests that the low latitude boundary layer may also be populated by solar wind particles [Song et al., 1994]. These simulated trajectories are quantitatively similar to the previous results from Richard et al., [1994] and Moore et al., [2005]. In particular, these ions from the solar wind enter the magnetosphere and form the low latitude boundary layer, near-Earth plasma sheet and ring current-like region around the Earth [Richard et al., 1994, Moore et al., 2005].

40

Figure 3.11: Density distribution in the equatorial (XY) plane, 3 hours (physical time) after starting the simulation.

3.2.3 Modelling results

As can be seen from simulated isolated trajectories, solar wind ions may penetrate the magnetosphere and drift to the tail region while following different possible routes. To further examine the population of the inner magnetosphere and the plasma sheet during northward IMF, the density distributions of particles, obtained with the calculation method introduced above, are shown as follows. The density unit in all figures corresponds to $1m^{-3}$.

The magnetosphere is initially empty, and particles are injected at a certain rate, for a certain period of physical time (around 9 hours in this case), until a steady state population is reached. Hereafter, all the time appearing in the figures corresponds to physical time. The density distribution calculated after 3 hours (physical time) in the equatorial (XY) plane is illustrated in Figure 3.11. The colored density profiles clearly reveal the shape of the bow shock,

41
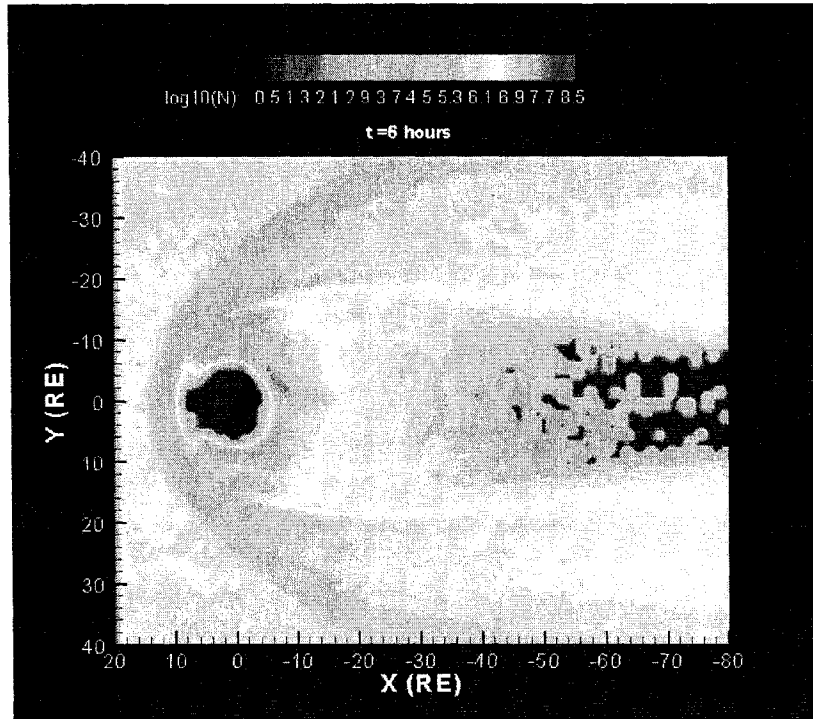
Figure 3.12: Density distribution in the equatorial (XY) plane, 6 hours (physical time) after starting the simulation.

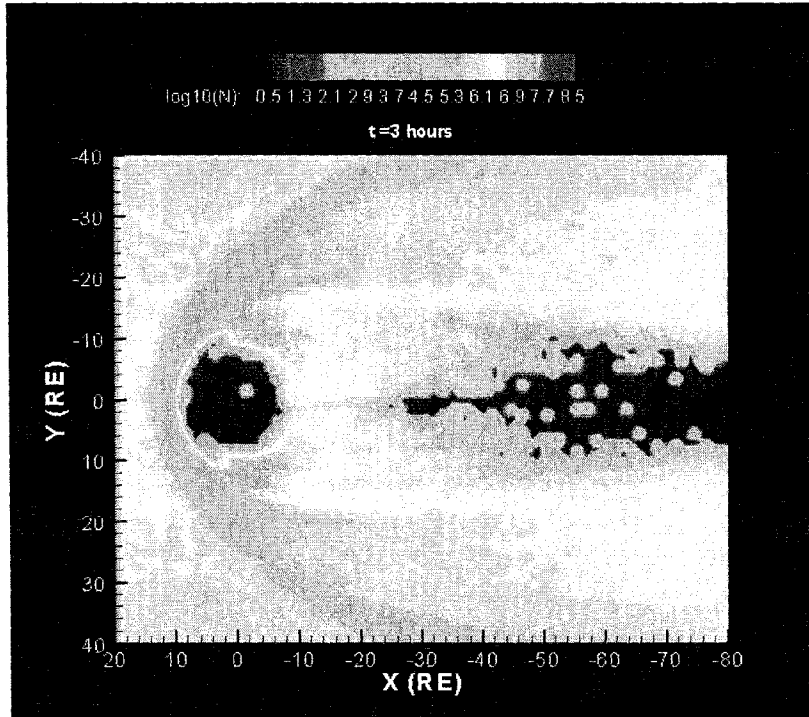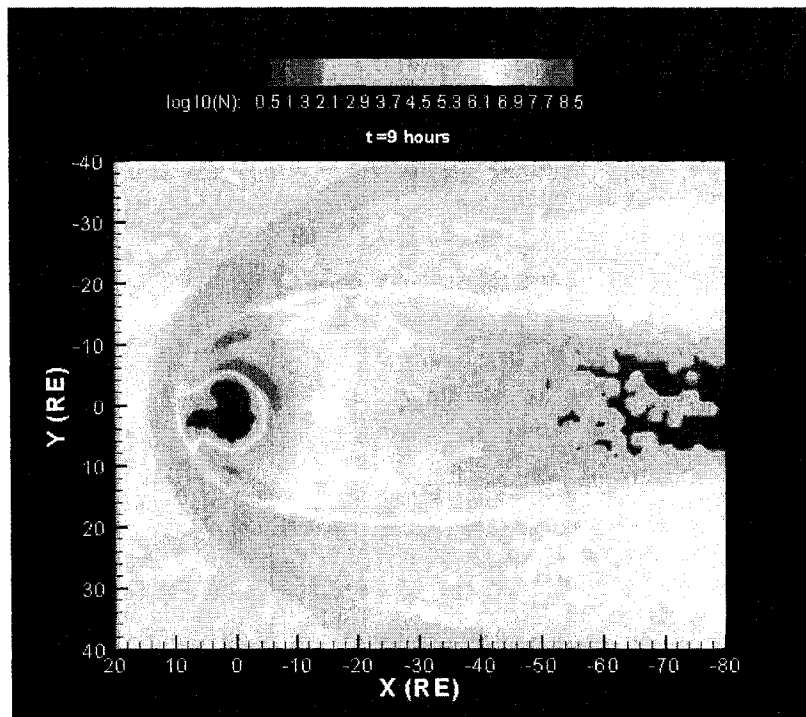Figure 3.13: Density distribution in the equatorial (XY) plane, 9 hours (physical time) after starting the simulation.

42
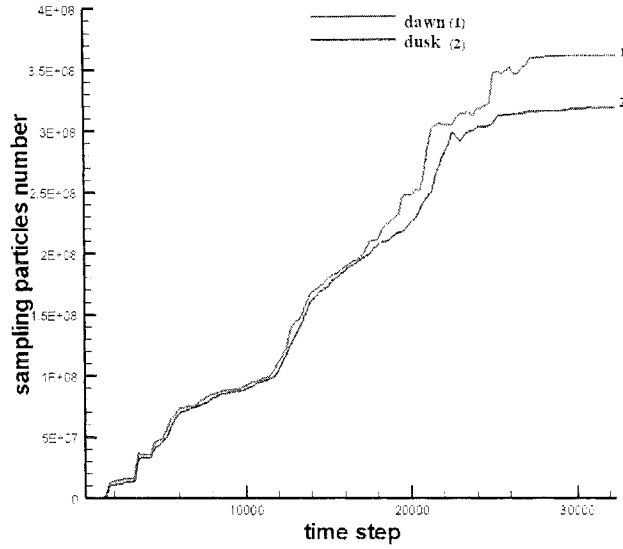
Figure 3.14: Total numbers of particles in the dusk and dawn flanks sampling regions, as a function of the simulation time step ($\Delta t = 1s$)

the magnetopause and the low latitude boundary layer in this simulation. The orange region in the dayside and distant tail shows the highly dense magnetosheath plasma coming from the solar wind. Consistent with the transport paths considered earlier, many magnetosheath particles penetrate the magnetopause and then populates the near-Earth plasma sheet and the low latitude boundary layer on both the dawn and dusk sides. The dense region along the flanks of the low latitude boundary layer implies that it is also an entrance region for magnetosheath plasma into the magnetosphere, in addition to the cusp [Richard et al., 1994, Song et al., 1994]. As shown in Figure 3.10 (physical time t=6 hours) and Figure 3.11 (physical time t=9 hours), more particles flow tailward and form the dense plasma sheet as time increases. The simulated density has an actual maximum close to the Earth and decreases as it extends to the tail. Although with a different colour scale, the configuration of the near-Earth plasma sheet density distribution agrees qualitatively with

43

the statistical results from the DMSP observation (Figure 3.2). In addition, a ring current-like region is formed around the Earth at approximately $8R_E$ from the centre of the Earth. It is also noticeable that the density peaks on the dawn side are larger than those on the dusk side, because some penetrating particles only drift at the dawn side and then flow into the tail without being trapped to the dusk side, as illustrated in Figure 3.9. Along with these density distributions, Figure 3.14 also shows the weak dawn-dusk asymmetry in the flank regions. This is apparent from the total particle number in sampling near-Earth dusk and dawn flank regions in the equatorial plane (defined as $-10R_E < X < 0, 10R_E < |Y| < 15R_E$). The total number of particles in these two regions increases as a function of time and the total number on the dawn side flank is larger than that on the dusk side, which is consistent with the results from observations cited above (see Figures 3.1 and 3.2). It is also clear that the total number of particles in these two regions become almost constant close to 9 hours (physical time), which confirms that the population of the inner magnetosphere reaches the steady state at this time.

In Figures 3.15, 3.16 and 3.17, the density distributions in the noon-midnight meridian plane (XZ) are shown, respectively, for the physical times t=3 hours, t=6 hours and t=9 hours. The configuration of the bow shock and magnetosheath are clearly identifiable in these figures. The cusp regions in both hemispheres are also visible. In addition to that, the large density in the high latitude reconnection region explains most of magnetosheath plasma entering through the cusp. However, considering the positive Earth dipole tilt angle in the simulation, particles preferably enter from the north-hemisphere, therefore the plasma in the north cusp is denser than that in the south one. At first, the penetrating particles flow to the nightside and populate the high latitude mantle region, and form a ring current-like region near the Earth

44

Figure 3.15: Density distribution in the noon-midnight meridian plane (XZ), 3 hours (physical time) after starting the simulation.

Figure 3.16: Density distribution in the noon-midnight meridian plane (XZ), 6 hours (physical time) after starting the simulation.

45
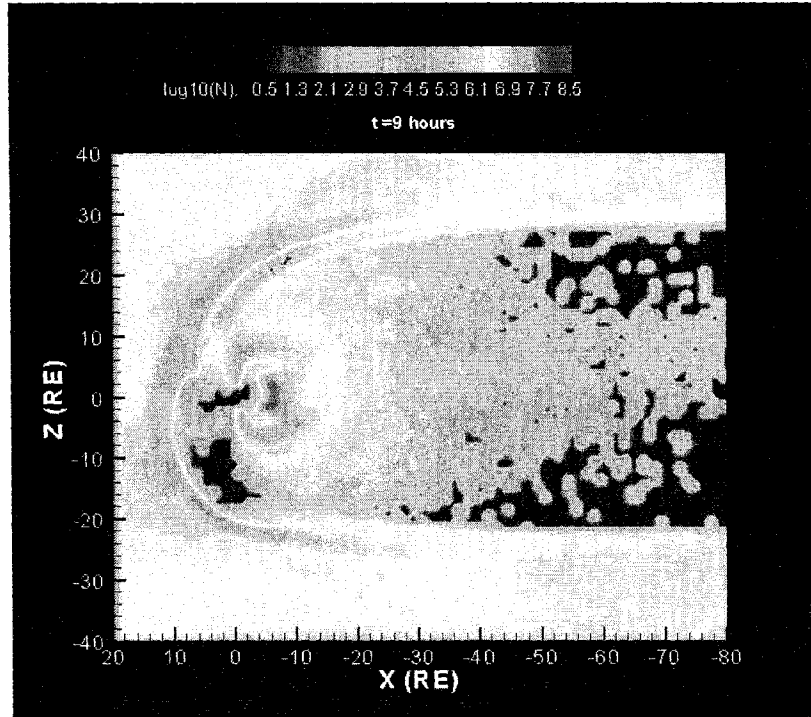
Figure 3.17: Density distribution in the noon-midnight meridian plane (XZ), 9 hours (physical time) after starting the simulation.

(Figure 3.15), where most trapped particles bounce and drift to the dayside. Eventually more particles come inside and flow into the high latitude mantle and the distant tail. The absence of clear plasma lobes makes it difficult to recognize the plasma sheet in this perspective. In Figure 3.17, the ring current-like region seems to be closer to the Earth than that at previous times. Also the density of ring current-like region at the nightside part is larger than that at the dayside, as a result that large numbers of particles in the dayside are lost back to the magnetosheath or the distant tail through the magnetospheric flanks.

From Figure 3.18 to 3.20, the density distributions at the dawn-dusk meridian (YZ plane at X=0) are shown respectively for the physical time t=3 hours, t=6 hours and t=9 hours. The outward orange ring region corresponds to the magnetosheath plasma. The outer boundary corresponds to the bowshock and
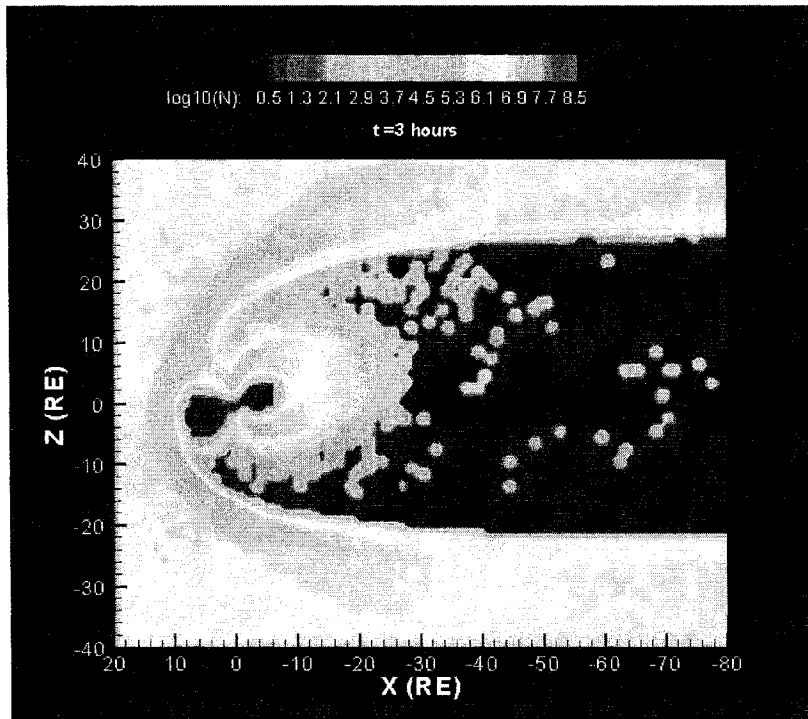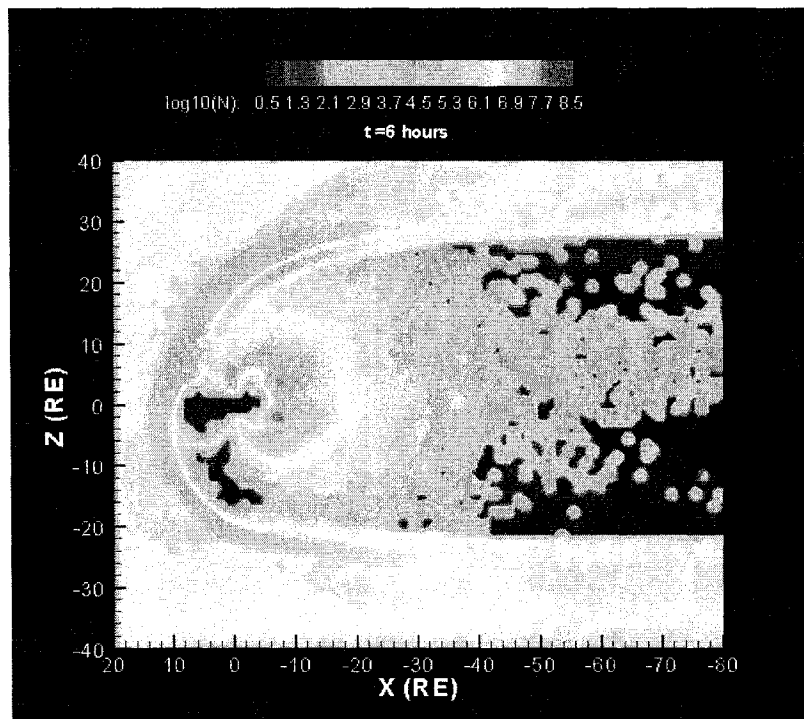
46
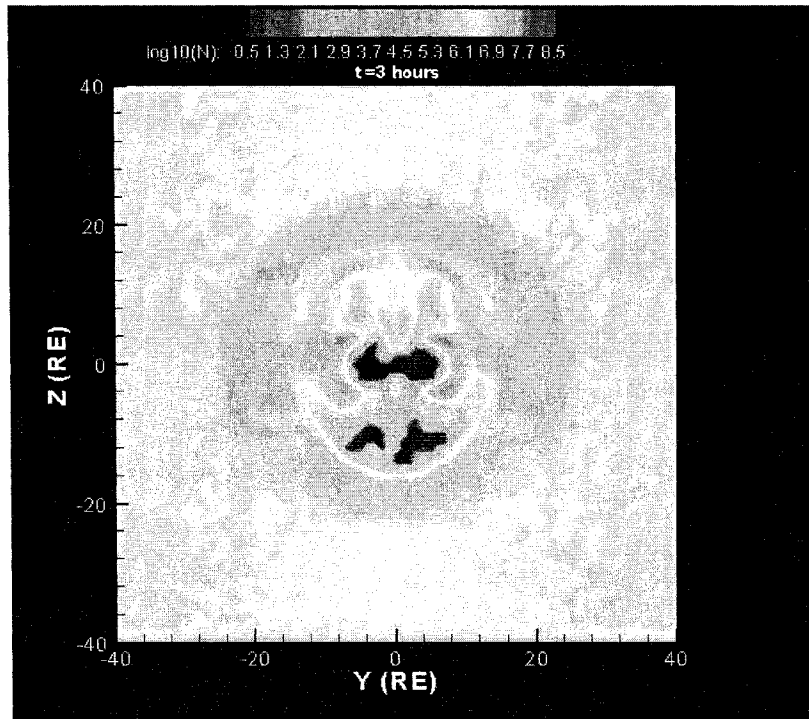
Figure 3.18: Density distribution in the dawn-dusk meridian (YZ plane at X=0), 3 hours (physical time) after starting the simulation.
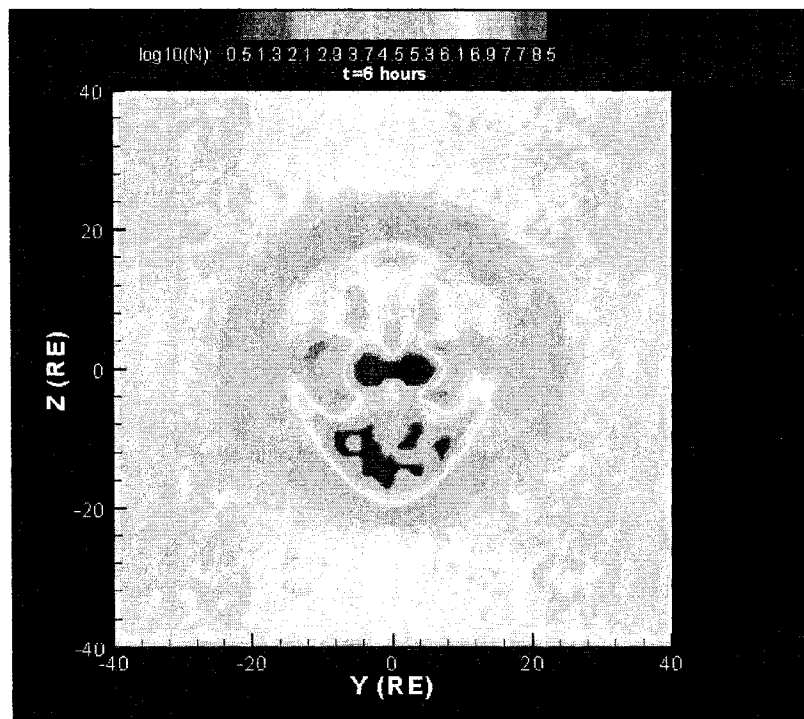
Figure 3.19: Density distribution in the dawn-dusk meridian (YZ plane at X=0), 6 hours (physical time) after starting the simulation.

47
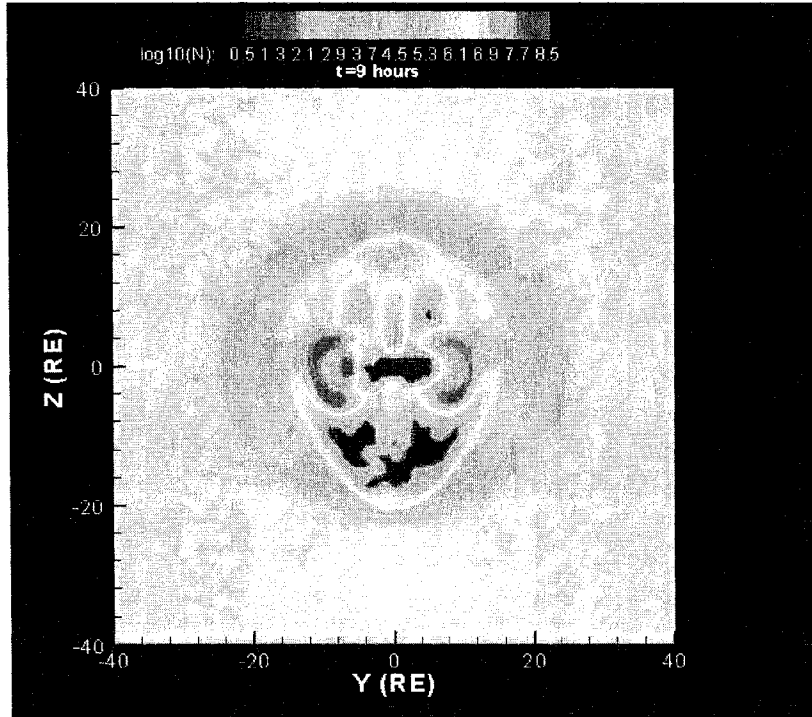
Figure 3.20: Density distribution in the dawn-dusk meridian (YZ plane at X=0), 9 hours (physical time) after starting the simulation.

the inner boundary corresponds to the magnetopause. The inside two valvular regions on the dawn and dusk sides are the cross section of ring current-like region as shown in the XY and XZ planes. The yellow part between the magnetopause and the ring-current like region corresponds to the low latitude boundary layer. These cross sections again illustrate the penetration of magnetosheath plasma through the cusp preferably in the north side. Also, the weak dawn-dusk asymmetry shown in these cuts is in conformity with the results shown on the equatorial plane (Figure 3.17).

To further illustrate how solar wind plasma populates the boundary layers and the plasma sheet during the northward IMF, the cross section of the near-Earth plasma sheet at $X = -30R_E$ is shown in Figure 3.21. It is clear that the plasma density decreases from the magnetosheath (orange region) to the boundary layer (yellow region) and to the magnetotail (green region).

48
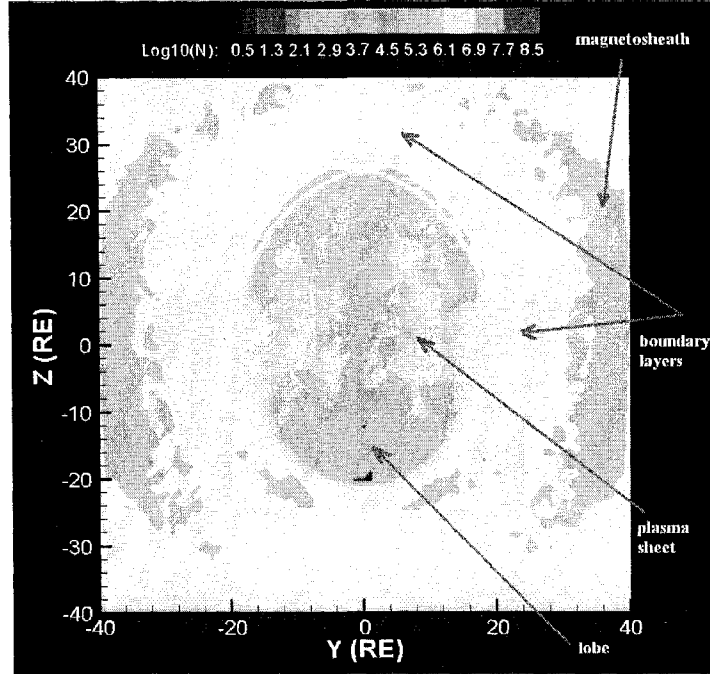
Figure 3.21: Density distribution in the cross section of the near Earth plasma sheet(YZ plane at $X = -30R_E$), 9 hours (physical time) after starting the simulation.

Table 3.2: Plasma density in different inner magnetospheric regions

Inner magnetospheric regions	Calculated density	Observed density
Magnetosheath	$\sim 10/cm^3$	$\sim 20/cm^3$
Boundary layers	$\sim 3.2/cm^3$	$0.1 \sim 10/cm^3$
Plasma lobes	$\sim 0.01/cm^3$	$\sim 0.01/cm^3$
Dense plasma sheet	$\sim 1/cm^3$	$\sim 1/cm^3$

Although the green region is not empty, it can be regarded as the plasma lobe since it has the lowest density. Inside the plasma lobe, a light yellow region can be identified, which is the dense plasma sheet with a density around $1cm^{-3}$. In Table 3.2, the density values of different regions in the inner magnetosphere are listed, which includes the approximate value from the simulation and the typical value from the observation. Comparing these results, the density values of the overall tail configuration obtained from the simulation are in agreement with the typical observed data.

49
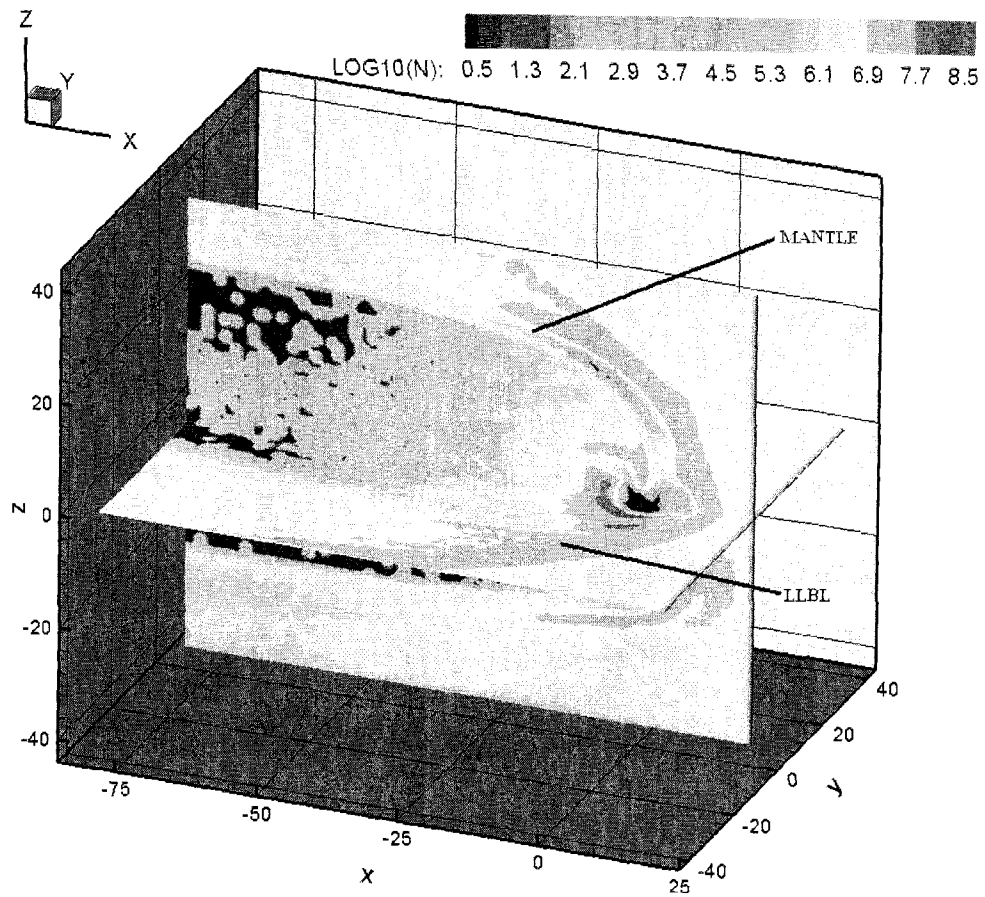
Figure 3.22: A three dimensional cutaway diagram of the particle density distribution looking from the dawn side, which illustrates the LLBL and plasma mantle formation.
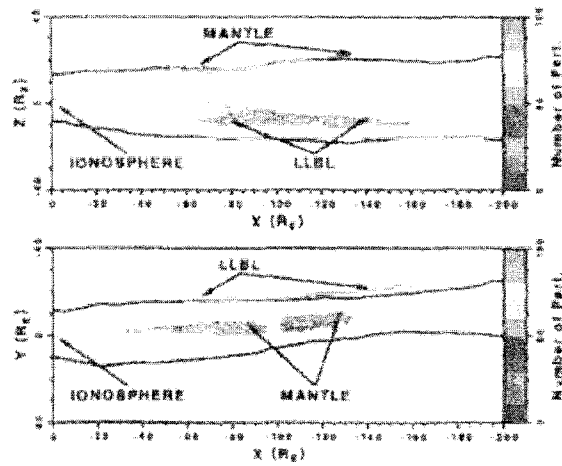
Figure 3.23: Illustration of the three main sources for the tail region reported by Ashour-Abdalla, using the large scale backward tracing [Ashour-Abdalla et al., 1997].

50

In this simulation of large scale transport processes, the majority of the solar wind plasma simply undergoes $\mathbf{E} \times \mathbf{B}$ drift through the flanks, into the distant tail without entering the inner magnetosphere. Nevertheless, the low latitude boundary layer and the high latitude mantle are significantly populated with the incoming flow from the magnetosheath with particles originating from the solar wind (see Figure 3.22). This result is consistent with another large scale kinetic simulation by Ashour-Abdalla, who uses backward tracing in time from the distant tail, and finds that the three main plasma sources for the tail region are the low latitude boundary layer, the high latitude mantle and the ionosphere (see Figure 3.23, from Ashour-Abdalla et al., [1997]). Because she does not consider only northward IMF, the ionospheric source exists in her simulation results. In addition, part of the penetrating particles are trapped around the Earth and form the ring current-like region, which has a larger density in the nightside, especially on the dawn side, and this configuration is similar to the geosynchronous (nonstorm) ring current region noted by Moore et al., [2005].

Chapter 4

Modelling electron response to sudden change in the solar wind dynamic pressure

4.1 Observations and Simulations of Energetic Particle Injections

As introduced in Chapter 1, dispersionless injections are generally associated with a rapid change of the magnetospheric configuration in a local time. There are several possible ways to trigger a transient change of the magnetospheric configuration, for example, a quick flip in the IMF orientation or an abrupt jump of the solar wind dynamic pressure. Energetic particle injections are also suggested as evidence for particles local acceleration. In a simple situation, assuming that the first adiabatic invariant $\mu = \frac{W_\perp}{B}$ is conserved during the transport process, particles are energized if they are injected into a region with larger magnetic field magnitude. In reality, the physical processes responsible for particle energization are many and more complex. For example, they may involve instabilities, wave-particle interactions or other dynamical processes.

Most observation of dispersionless injections, associated with substorm events, are made around the geosynchronous orbit, approximately at $6.6R_E$ geocentric distance in the equatorial plane [Baker et al., 1982, Birn et al., 1997].
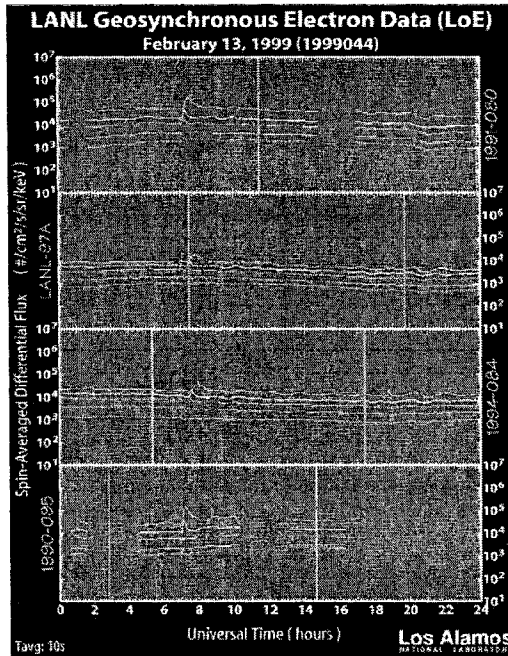
Figure 4.1: Example of the observed dispersionless injection from the Los Alamos National Laboratory, Geosynchronous Energetic Particle Data.

Figure 4.1 shows an example of electron injection data from the geosynchronous energetic particle data of Los Alamos National Laboratory. This observation is made for the substorm event of February 13, 1999. From top to bottom, the four plots represent geosynchronous satellites 1981-080, LANL-97A, 1994-084 and 1990-085, respectively. Each of them has six electron channels with different energy ranges: 50-75KeV, 75-105KeV, 105-150KeV, 150-225KeV, 225-315KeV and 315-500KeV. As the dipolarization occurred between 7 and 8 hours (universal time), the electron flux for all energy channels increases suddenly almost simultaneously, which represents the dispersionless injection. The geostationary satellites also observe the electron injections, characteristic of the dispersionless injection, during a nonstorm time associated with the solar wind pressure pulse [Lee and Lyons, 2004, Lee et al., 2004].

Energetic electron injections associated with dipolarization events have been studied extensively with different simulation models. For example, Li.

53

et al., [1998, 2003] use the dipolarization pulse model, with an empirical time-varying analytic magnetic field (with only Z-component) and the azimuthal electric field, to investigate the electrons transport in the equatorial plane in the guiding centre approximation. Another approach is to use a drift test particle code coupled with a global MHD models [Birn et al., 1998, Kim et al., 2000]. In Li's model, the electrons, initially distributed around the Earth, are affected by a strong earthward radial transport with $\mathbf{E} \times \mathbf{B}$ drift in the dipolarization region. In Birn and Kim's models, they simulate the substorm event by quick flipping the IMF orientation from southward to northward, and electrons are distributed initially at the plasma sheet region. As the substorm proceeds, the electrons also drift to the Earth because of earthward radial transport in the nightside. Their results successfully reproduce the dispersionless injections in a local time. In this chapter, electron response to a transient dipolarization-like process, triggered by a sudden decrease in the solar wind dynamic pressure, is considered. Use is made of a test particle code with time-dependent magnetic and electric fields obtained from the global MHD model BATS-R-US, [Powell et al., 1999].

4.2 Modelling

4.2.1 Modelling method

In this study, electron transport is considered in the near-Earth region. This region is close to being dipolar, and its electrons are well magnetized. Therefore, it is possible to consider particle trajectories in the guiding centre approximation. The drift equations for electrons are the same as the ones presented in Chapter 2 for ions. In this case, the simulation domain is the rectangular prism made of 141 by 121 by 61 nodes, delimited by $-50R_E \leq x \leq 20R_E$, $-30R_E \leq y \leq 30R_E$, and $-30R_E \leq z \leq 30R_E$ in the GSM coordinate system.

54

The spatial resolution in the x and y directions is $0.5R_E$, and it is $1R_E$ in the z direction. The time step used for tracing electrons is 0.02 second. Initially, 2,000,000 electrons are distributed randomly in a ring region in the equatorial plane with radial distances ranging between $3R_E$ and $10R_E$. Their energies are initialized with a Kappa distribution into four energy ranges: 75-105KeV, 105-150KeV, 150-225KeV and 225-500KeV, using 500,000 electrons for each energy channel. For simplicity, the pitch angles of all electrons are set to be 90°. This simplification is deemed sufficient for the purpose of modelling transport on the equatorial plane. The simulation is time-dependent and it is carried over the whole period which characterizes the injection progress. Before starting the time-dependent simulation, however, it is necessary to initialize the electron distribution by gradually injecting electrons in the simulation domain until a stationary distribution is obtained. After this initialization, the electrons are followed in the time-varying electric and magnetic fields as prescribed by BATS-R-US. In this simulation, particles are removed wherever they exit the simulation domain. Note that while lost particles are continuously reinjected in the steady state initialization phase of the simulation as they exist the simulation domain, they are not reinjected in the time-dependent part.

As in other simulations of electron injections [Li et al., 1998, Li et al., 2003, Mithaiwala and Horton, 2005], the initial electron energy distribution in the ring region is chosen to follow a Kappa distribution [Vasyliunas, 1968]

$$j(E_i) = j_0 \frac{(1 + \frac{1}{\kappa})^{1+\kappa}}{E_\kappa} \frac{E_i}{(1 + \frac{E_i}{\kappa E_\kappa})^{1+\kappa}}. \tag{4.1}$$

where $j(E_i)$ is the differential flux and E_i is the particle's energy, and other parameters are the same as those used by Mithaiwala and Horton, [2005],

55

namely $\kappa = 3.5$, $E_\kappa = 1.14 KeV$, $j_0 = 5.5 \times 10^6 cm^{-2} s^{-1} sr^{-1} KeV^{-1}$. Based on this Kappa distribution, each electron i injected in the simulation domain is given a weight factor $j(E_i)$ to represent its contribution to the differential flux calculation. This weight factor is then carried by each particle through the simulation, and it is used to provide an absolute calibration of energy fluxes as particle transport and energization take place.

The individual electron positions, velocities and energies are recorded at each time step. Using this information, the differential flux can be calculated by applying Liouville's theorem [Walt, 1994]. Liouville's theorem provides the relationship between the particle phase space density f and the differential flux j,

$$ f = \frac{j}{p^2} \propto \frac{j}{(\gamma + 1)E}, \tag{4.2} $$

where p is the particle momentum and E is the particle energy. It states that the phase space density f is conserved along a dynamical trajectory of particle. Therefore, if the particle's initial flux j_i and energy E_i are known, it is possible to calculate its differential flux j_f at a later time and particular position from its final energy E_f, as

$$ j_f = j_i \frac{E_f}{E_i} \frac{\gamma_f + 1}{\gamma_i + 1}. \tag{4.3} $$

The individual particle's flux contribution is obtained from Equations 4.1 and 4.3 when the particle crosses the equatorial plane. The total flux distribution in the equatorial plane is then calculated using the methodology

56

introduced in Chapter 3.

4.2.2 Simulation results

As stated earlier, the background field configuration is obtained from the global MHD model (BATS-R-US). The simulated physical time period is 12 minutes. The time-dependent background MHD fields are obtained from linear interpolations of seven BATS-R-US simulation files, two minutes apart. As with time-independent simulation in Chapter 3, these MHD files are also transformed from the unstructured mesh in BATS-R-US to the structured mesh in the test particle code by interpolation.

The previous statistical study by Lee and Lyons [Lee and Lyons, 2004] shows that stronger changes in the solar wind pressure result in higher compressions of the dayside magnetic field. In order to provide the field configuration with rapid change for this simulation, a steady state field configuration with high solar wind dynamic pressure (the solar wind speed is 400 km/s and its density is $5cm^{-3}$) is obtained first. Then the solar wind dynamic pressure is suddenly decreased with a factor of 10 (the solar wind speed changes to 200 km/s and its density changes to $1cm^{-3}$). The response of this rapid change is simulated by using BATS-R-US. Figure 4.2 shows the magnetic field lines configurations at three different physical times ((a)t=0, (b)t=4 minutes, (c)t=12 minutes) from the BATS-R-US simulation. The interplanetary magnetic field is northward during the whole simulation. The background contour distribution is about solar wind density, which is decreasing from plot(a) to plot(c), together with the decreasing dynamic pressure. It is clear that the magnetic field configuration is compressed on the dayside as time increases. At the same time, the stretched field configuration in the nightside expands and becomes more dipolar-like, which is a dipolarization-like process. During this transient

57
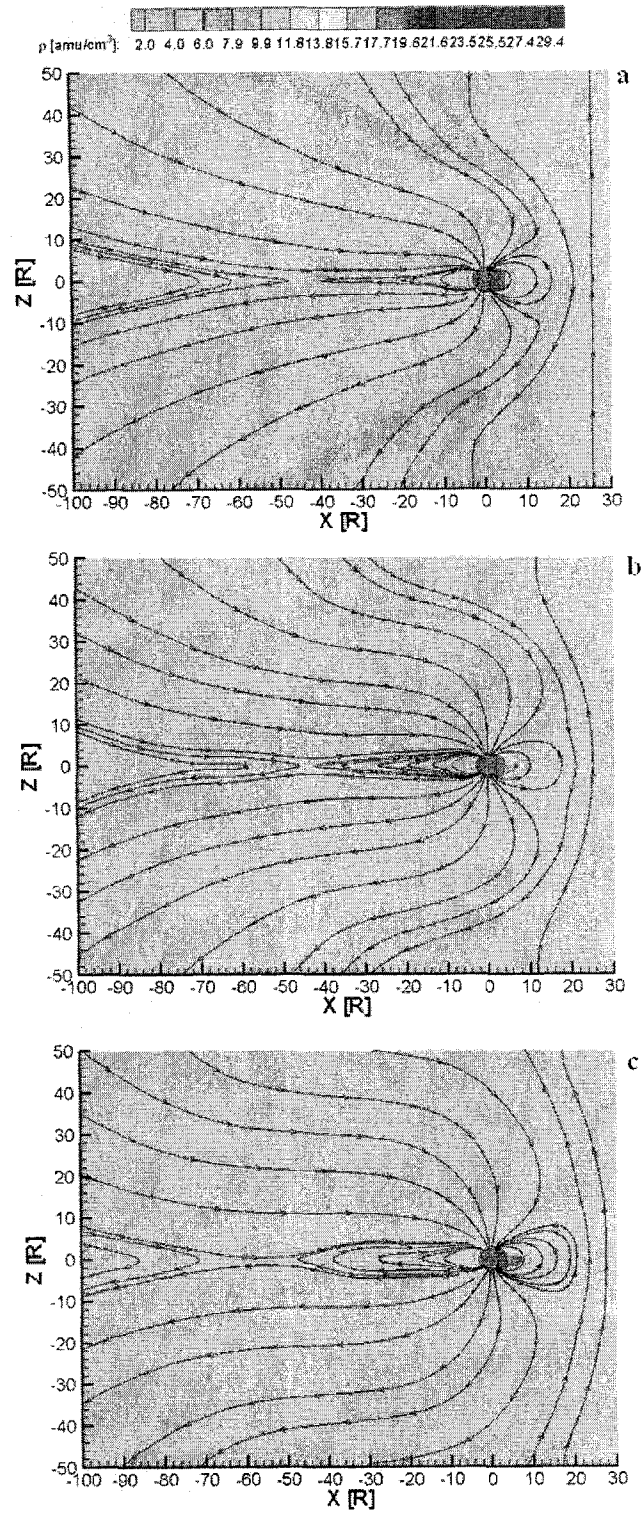
Figure 4.2: The MHD simulation result of the magnetic fields configuration during the transient process associated with solar wind pressure decrease from the MHD simulation. (a)t=0, (b)t=4 minutes, (c)t=12 minutes.

58
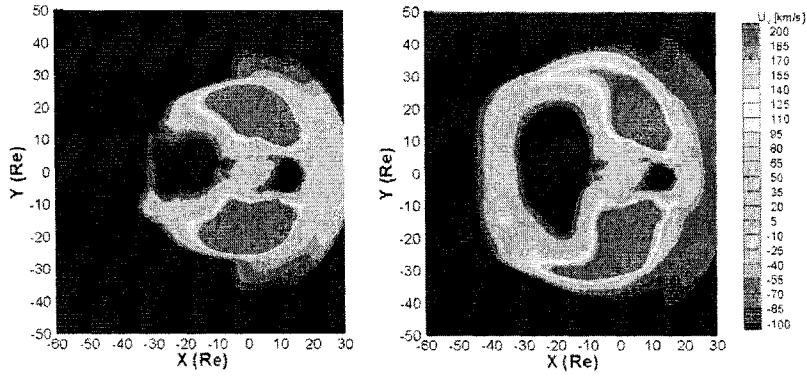
Figure 4.3: The MHD simulation result of X-component of the plasma flow velocity during the transient process associated with solar wind pressure decrease, left panel is at t=4 minutes, right panel is at t=12 minutes.

process, particles are expected to be redistributed and accelerated, which lead to the flux enhancements, characteristic of dispersionless injection.

During the typical dipolarization process, two kinds of plasma flows may exist in the magnetosphere. One is the earthward plasma flow in the near-Earth region, and the other is the tailward plasma flow in the tail region. In previous studies [Birn et al., 1998, Kim et al., 2000], it is found that the earthward plasma flow, resulting from the induced electric fields, accounts for the energetic particle injections from the near-Earth plasmasheet. The plasma flow obtained from the BATS-R-US is illustrated in Figure 4.3 at two times of the simulated dipolarization-like event. It shows the X-component (Sun-Earth direction) profile of the plasma flow velocity in the equatorial plane. As seen in the left panel of Figure 4.3, the weak earthward plasma flow is generated at the $X=-30R_E$ when the solar wind pressure is decreased (t=4 minutes). After the rapid change of pressure (t=12 minutes), the range of the earthward plasma flow becomes larger (between $X=-40R_E$ and $X=-30R_E$, right panel of Figure 4.3) without extending to the near-Earth region, which suggests that the dipolarization-like process studied here does not have the similar flow structure as the typical dipolarization event. Nonetheless, the

59
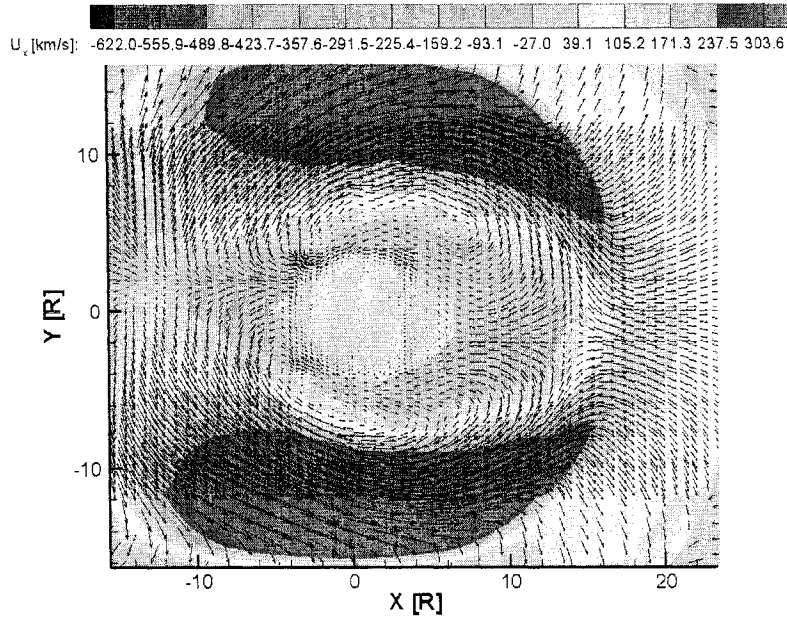
Figure 4.4: Flow vectors at the initial time t=0.

magnetic compression on the dayside must influence the particle motions and lead to flux change.

In this study, all the electrons are initially distributed within $10R_E$ from the Earth. Therefore, the effect of the plasma flow around this region is more important than that in the tail region. In the equatorial plane (without considering the parallel velocity), electrons perform two kinds of drift motions: grad-B drift and $\mathbf{E} \times \mathbf{B}$ drift. As discussed in Chapter 3, the $\mathbf{E} \times \mathbf{B}$ drift motion, resulting from the induced electric fields, has the same streamline configuration as the plasma flow in the equatorial plane (see Equation 3.7). In order to better understand its effect on the electrons injection, the plasma flow velocity profiles, obtained from BATS-R-US, in the equatorial plane are illustrated in Figures 4.4, 4.5, 4.6. In these figures, the contour background gives the distribution of the X-component flow velocity, and the black arrows represent the flow vectors in both direction and magnitude.

60
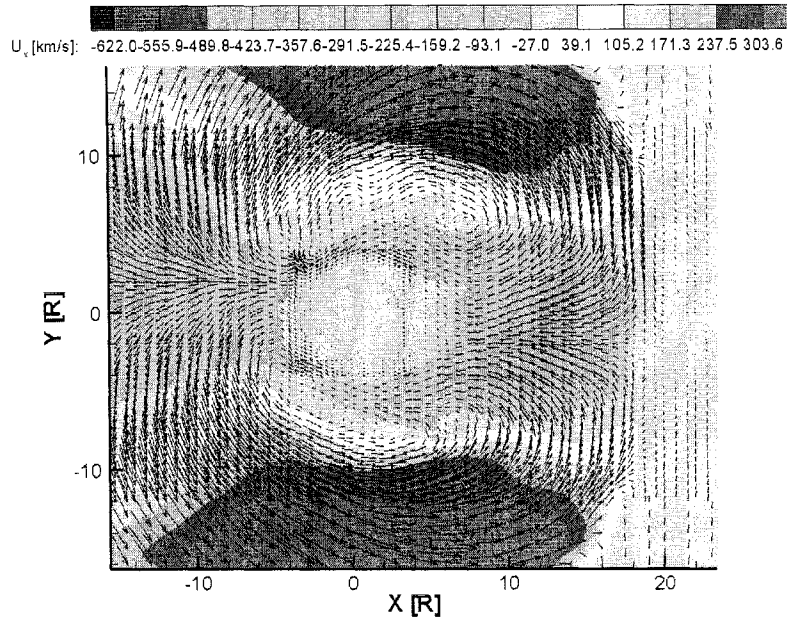
Figure 4.5: Flow vectors when the dayside magnetosphere begins compressing, at t=4 minutes.
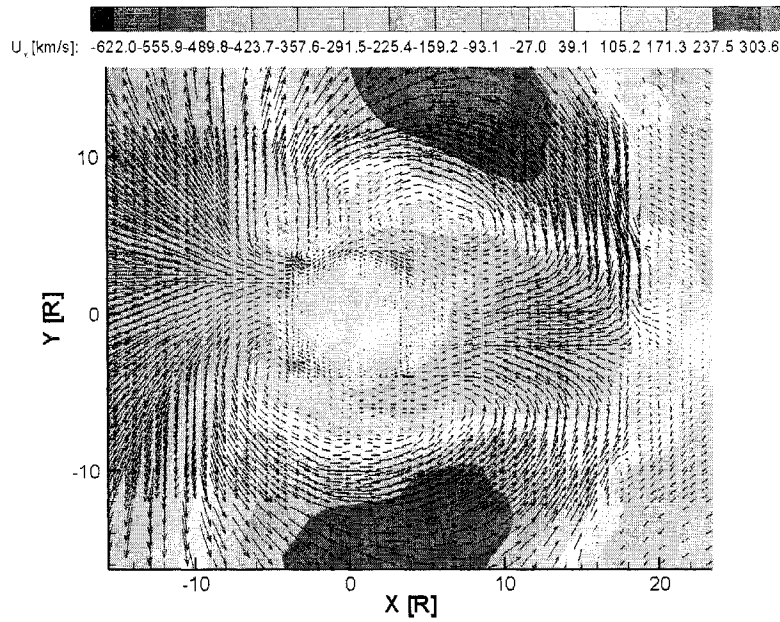
Figure 4.6: Flow vectors of the last MHD output, at t=12 minutes.

61

Figure 4.4 shows the flow vector field at the initial time (t=0). The plasma flow in the nightside is tailward. From there, electrons may drift to either the dawn or dusk side with the outward flow. In the dawn and dusk regions, the plasma flow is sunward. With this very strong flow and grad-$\mathbf{B}$ drift, electrons may drift to the dayside, and then some electrons may drift back toward the Earth. Other electrons may drift outward and be lost at the outer boundary. Figure 4.5 shows the flow vectors when the compression of magnetosphere appears on the dayside (t=4 minutes), triggered by solar wind pressure decrease. The plasma flow in the nightside is still tailward and even stronger. However, the circulation pattern of the plasma flow on the dayside is changed considerably as a result of the compressed magnetic field. All the plasma flow is earthward on the dayside and is comparatively stronger than that before the compression. Therefore, during magnetic field compression, almost all the electrons drifting to the dayside may be energized resulting from the earthward flow, which accounts for the energetic electron injection. Figure 4.6 shows the flow vectors at the last time (t=12 minutes). The plasma flow on the nightside and dayside are all tailward and earthward respectively. The flow on the dawn and dusk regions, however, becomes weaker. On the dayside, there is a small region with outward flow, and its effect on particle transport is negligible compared with that of the strong earthward flow. In these illustrations, all the dayside effect is due to the sudden decrease of solar wind pressure.

To further illustrate the effect of the $\mathbf{E} \times \mathbf{B}$ drift on the electrons motion, Figure 4.7 shows some sample trajectories of the electrons starting from the nightside, with initial positions at $X = -5.5R_E$, $X = -7.5R_E$, $X = -9.5R_E$. These electrons are launched with initial energies of 90KeV (label 1), 120KeV (label 2), 180KeV (label 3) and 350KeV (label 4), which fall within the four simulated energy channels, and they are traced for 10 minutes (physical time).
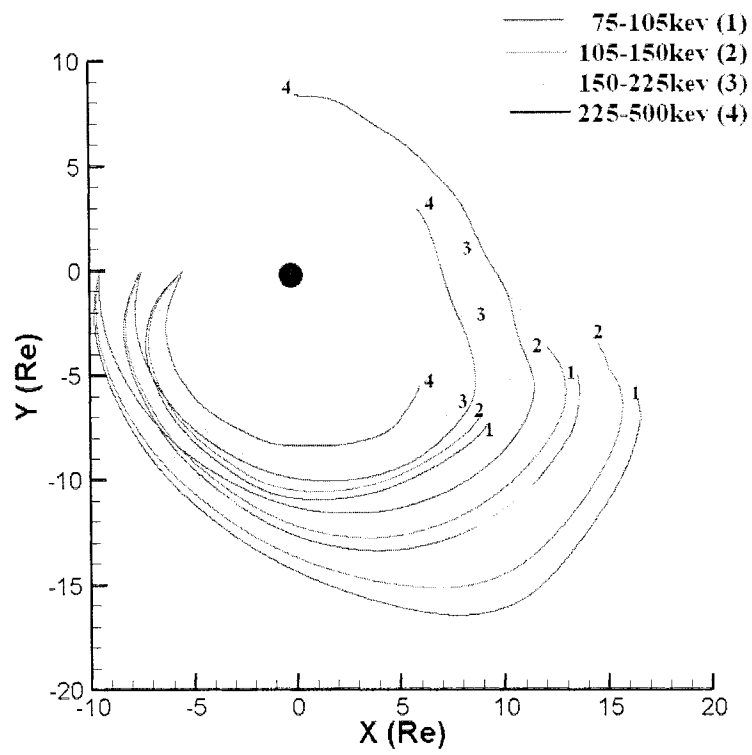
62

Figure 4.7: Example electron trajectories starting from the nightside

63

All electrons move eastward because of the grad-**B** drift. As in the previous discussions, because of the strong outward $\mathbf{E} \times \mathbf{B}$ drift on the dawn side, all these electrons initially drift away from the Earth. The low energy electrons drift further out than the high energy ones. Also the outward moving trend is more pronounced for the electrons initially in the outer regions, with larger radial excursions, than those in the inner regions. During their outward drift, all electrons are decelerated because their magnetic moment is conserved, while the magnitude of the local magnetic field decreases. As mentioned above, the dayside flow configuration turns to being entirely earthward during the magnetic field compression process. Therefore, all these electrons are accelerated while drifting back toward the Earth, when they arrive at the dayside region. The results seen with these sample trajectories suggest that electron injection may be observed, and the differential fluxes may change during the dayside compression process.

The following considers the time dependence of the energy fluxes obtained from the test particle code. A simulation is made for a period of 14 minutes (physical time) including all MHD time-dependent fields. The electron fluxes for the four energy ranges are calculated every time step (0.02 second), and then are averaged over a period of 6 seconds (physical time) in order to reduce statistical noise. The result is therefore 140 output flux files with time resolution of 6 seconds. The time-dependent electron fluxes for all four energy ranges are presented in Figure 4.8. The electron fluxes are integrated in ring regions from $8R_E$ to $10R_E$(Figure 4.8a), from $6R_E$ to $8R_E$(Figure 4.8b) and $4R_E$ to $6R_E$(Figure 4.8c) in the equatorial plane. The results plotted on the Y axis are the logarithm of the calculated electron differential fluxes. The red, green, yellow, blue curves correspond to 75-105KeV (label 1), 105-150KeV (label 2), 150-225KeV (label 3), 225-500KeV (label 4) respectively.
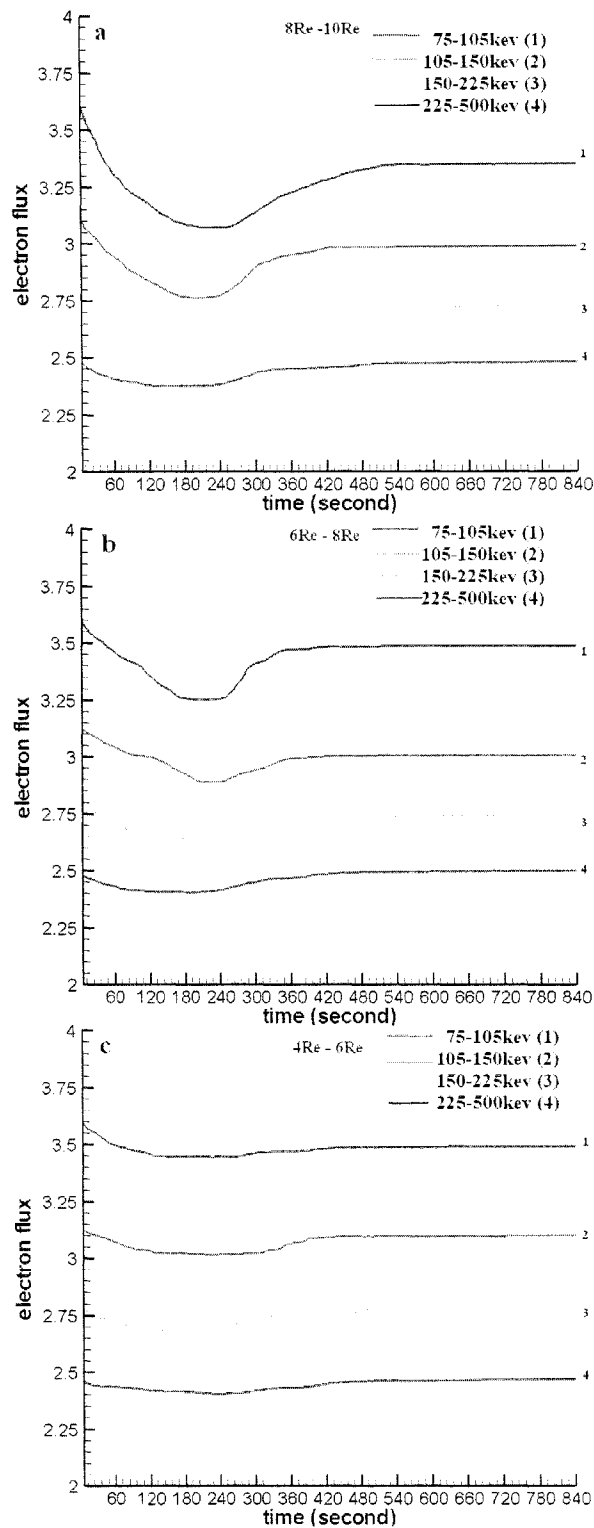
64

Figure 4.8: Logarithm of the calculated electron differential fluxes $(cm^{-2}s^{-1}sr^{-1}KeV^{-1})$ in different energy ranges, in three regions: a $(8R_E,10R_E)$, b$(6R_E,8R_E)$, c$(4R_E,6R_E)$

65

In Figure 4.8a and 4.8b, the temporal evolution of electron fluxes are similar. For a given energy range, each electron flux starts by decreasing because some electrons are decelerated while drifting outward in either the dawnside or the duskside, as illustrated in Figure 4.4. This results from the strong $\mathbf{E} \times \mathbf{B}$ drift in these regions. With the appearance of the dayside compression, all the electron fluxes, with different energy channels, begin increasing at approximately the same time (t=240 seconds), which constitutes the dispersionless injection. This increase in the fluxes is due to the electrons on the dayside being transported and accelerated toward the Earth, as illustrated in the sample trajectories (see Figure 4.7). It can be understood from Figure 4.6 that the plasma flow configuration does not change obviously except for the flow at the dawn and dusk regions becomes weaker after the sudden decrease of solar wind pressure. This is consistent with the reduction in the growth of electron fluxes following the simultaneous increasing. The electron flux of the highest energy range (225-500KeV) shows less variations than that of the others. This may be due to relatively fewer electrons being accelerated to the highest energy channel during this transient transport. The grad-$\mathbf{B}$ drift velocity for the high energy electrons is also much larger than the $\mathbf{E} \times \mathbf{B}$ drift velocity. As a result, the high energy electrons do not drift as far away from the Earth as low energy electrons and their radial transport is weaker at the dayside, which is shown in the sample trajectories in Figure 4.7. Therefore, their variations in energy are accordingly less distinct.

It is apparent from Figure 4.8c that there is no obvious fluctuation in the electron fluxes in the region close to the Earth ($4R_E$ to $6R_E$). Some electrons may drift outward, especially those with low energy (see Figure 4.4). It is also possible for some accelerated electrons to arrive in this region, because of the earthward radial transport on the dayside. Nevertheless, most of the electrons

66

in this region undergo grad-$\mathbf{B}$ drift around the Earth. The influence of $\mathbf{E} \times \mathbf{B}$ drift in the near-Earth region is not as strong as that in the outer regions.

In this BATS-R-US simulation of a transient process triggered by solar wind dynamic pressure decrease, the nightside magnetic field configuration is dipolarization-like. However, the dipolarization is weak and is not the dominant process leading to radial transport toward Earth. The only earthward transport region is obtained on the dayside in this simulation. In future, dipolarization process associated with substorm events will be studied, in order to better understand dispersionless injections. Nonetheless, the solar wind pressure pulse studied in this thesis, is shown to produce the main features of global electron response (energetic electron injections), which is qualitatively consistent with many observations of nonstorm time injection associated with solar wind pulse [Lee et al., 2004, Lee and Lyons, 2004].

Chapter 5

Conclusion

5.1 Summary and Discussion

Simulation results of two case studies, obtained from the test particle code coupled with a global MHD model, have been reported in this thesis. The first case simulates solar wind plasma transport into the magnetosphere during northward IMF. The second case simulates energetic electron injection during a transient process associated with solar wind pressure decrease. The global MHD model, BATS-R-US, is used to provide the background electric and magnetic fields for test particle tracing. The simulations based on the guiding centre approximation prove to be numerically efficient, and yield results that are in qualitative agreement with observations.

In the first case, the simulation of solar wind mass transport has succeeded in reproducing many of the basic features of the Earth magnetosphere. It also provides a detailed picture of the entrance mechanism for the magnetosheath plasma that originates from the solar wind. During northward IMF, solar wind has been identified as the dominant source of magnetospheric plasma. The main route for solar wind plasma penetrating into the inner magnetosphere is through the high latitude tailward cusp region. Particles then transport to the magnetospheric flanks and are swept into the plasma sheet. Another

68

suggested entry path is from the low latitude boundary layer along the flanks, followed by a drift into the plasma sheet region. The qualitative agreement between observation (see Figure 3.2) and simulation (see Figure 3.15) on the near-Earth region in the equatorial plane is satisfactory. The precise physical mechanisms for the transport of particles through the flanks and the formation of cold dense plasma sheet are still an active area of research. Nevertheless without considering the effect of diffusion, the results presented here show that entry through the high latitude cusp is an important mechanism for populating the dense plasma sheet and magnetospheric boundary layers during the geomagnetic quiet time.

In the second case, electron injection associated with solar wind pressure decrease is considered. The test particle code is shown to be capable of simulating the electron response to a rapidly varying configuration of the magnetosphere. The model is successful at simulating the adiabatic transport of electrons and reproducing some general features of energetic electron injections. The results also suggest that the earthward radial $\mathbf{E} \times \mathbf{B}$ drift, resulting from the induced electric fields, play an important role in particles transport and energization during the dipolarization-like process associated with solar wind pressure pulse, as noted by other simulations of dipolarization events [Li et al., 1998, Li et al., 2003, Mithaiwala and Horton, 2005].

5.2 Future Efforts

Computer simulation models of the type presented in this thesis offer a powerful tool to predict and understand the complicated dynamic processes in the Earth's magnetosphere or that of other planets. With the development of advanced models and computing facilities, global MHD simulations will eventually provide more realistic and detailed configurations of the magnetosphere

69

for various geomagnetic conditions. Building on that forecasting frame, two kinds of research orientations can be investigated with test particle simulations in the future.

First, the model applicability can be broadened by solving the full Lorentz kinetic equations instead of the guiding centre equations. In simulations based on the guiding centre approximation, particle tracing is stopped when their motions are not adiabatic. However, if the study focuses on the particles energization process in a large region, it will be necessary to account for the nonadiabatic effects. The full Lorentz calculation has already been included in this code. It has been tested and can be applied to study the complicated dynamic processes over the broad magnetospheric regions.

Secondly, the test particle model is also capable of exploring the source and strength of magnetospheric plasma by tracing particle trajectories backward in time with realistic particle distributions in the magnetotail or in other regions obtained from observation. In addition, by using more precise field configurations including the non-MHD drift effect from other models coupled with the global MHD model, the test particle approach can be used to investigate particle energization and momentum exchange during storm and substorm events.

70

Bibliography

[Ashour-Abdalla et al., 1993] Ashour-Abdalla, M., and et al. (1993). Shaping of the magnetotail from the mantle: Global and local structuring. *J. Geophys. Res.*, 98:5651.

[Ashour-Abdalla et al., 1997] Ashour-Abdalla, M., and et al. (1997). Ion sources and acceleration mechanisms inferred from local distribution functions. *Geophys. Res. Lett.*, 24(8):955.

[Baker et al., 1982] Baker, N., D., and et al. (1982). Observations and modelling of energetic particles at synchronous orbit on July 29, 1977. *J. Geophys. Res.*, 87:5917.

[Birn et al., 1997] Birn, J., and et al. (1997). Characteristic plasma properties during dispersionless substorm injections at geosynchronous orbit. *J. Geophys. Res.*, 102:2309.

[Birn et al., 1998] Birn, J., and et al. (1998). Substorm electron injections: geosynchronous observations and test particle simulations. *J. Geophys. Res.*, 103:9235.

[Cummings et al., 1968] Cummings, D., W., Barfield, J. N., and Coleman, P. J. (1968). Magnetospheric substorms observed at the synchronous orbit. *J. Geophys. Res.*, 73:6687.

[Delcourt et al., 1994] Delcourt, C., D., Moore, T. E., and Chappell, C. R. (1994). Contribution of low-energy ionospheric protons to the plasma sheet. *J. Geophys. Res.*, 99(A4):5681C5690.

[Dungey, 1961] Dungey, J. W. (1961). Interplanetary magnetic field and the auroral zones. *Phys. Rev. Let.*, 6:47.

[Elkington et al., 2002] Elkington, R., S., and et al. (2002). MHD/particle simulations of radiation belt dynamics. *Journal of Atmospheric and Solar-Terrestrial Physics*, 64:607.

[Fujimoto and et al., 1998] Fujimoto, M. and et al. (1998). Plasma entry from the flanks of the near-earth magnetotail: Geotail observations. *J. Geophys. Res.*, 103:4391.

[Fujimoto and Terasawa, 1994] Fujimoto, M. and Terasawa, T. (1994). Anomalous ion mixing within an MHD scale kelvin-helmholtz vortex. *J. Geophys. Res.*, 99:8601.

[Hasegawa et al., 2004] Hasegawa, H., Fujimoto, M., Saito, Y., and Mukai, T. (2004). Dense and stagnant ions in the low-latitude boundary region under northward interplanetary magnetic field. *Geophys. Res. Lett.*, 31(L06802):doi:10.1029/2003GL019120.

[Kim et al., 2000] Kim, H., Chan, A. A., Wolf, R. A., and Birn, J. (2000). Can substorms produce relativistic outer belt electrons? *J. Geophys. Res.*, 105:7721.

[Lee et al., 2004] Lee, D.-Y., Hwang, J., Lee, E., Min, K., Han, W., and Nam, U. (2004). How are storm time injections different from nonstorm time injections? *Journal of Atmospheric and Solar-Terrestrial Physics*, 66.

[Lee and Lyons, 2004] Lee, D.-Y. and Lyons, L. R. (2004). Geosynchronous magnetic field response to solar wind dynamic pressure pulse. *J. Geophys. Res.*, 109:A04201, doi:10.1029/2003JA010076.

[Li et al., 1998] Li, X., Baker, D. N., Temerin, M., Reeves, G. D., and Belian, R. D. (1998). Simulation of dipersionless injections and drift echoes of energic electrons associated with substorms. *Geophys. Res. Lett.*, 25:3763.

[Li et al., 2003] Li, X., Sarris, T. E., Baker, D. N., Peteron, W. K., and Singer, H. J. (2003). Simulation of energetic particle injections associated with a substorm on august 27, 2001. *Geophys. Res. Lett.*, 30(1):doi:10.1029/2002GL015967.

[Lockwood, 1995] Lockwood, M. (1995). Overlapping cusp ion injections: An explanation invoking magnetopause reconnection. *Geophys. Res. Lett.*, 22(9):1141.

[Minsky and Papert, 1971] Minsky, M. and Papert, S. (1971). On some associative, parallel and analog computations. In Jacks, E. J., editor, *Associative Information Technologies*. Elsevier North Holland.

[Mithaiwala and Horton, 2005] Mithaiwala, M. J. and Horton, W. (2005). Substorm injections produce sufficient electron energization to account for mev flux enhancements following some storms. *J. Geophys. Res.*, 110:doi:10.1029/2004JA010511.

[Moore et al., 2005] Moore, E., T., and et al. (2005). Plasma sheet and (non-storm) ring current formation from solar and polar wind sources. *J. Geophys. Res.*, 110(A02210):doi:10.1029/2004JA010563.

[Northrop, 1963] Northrop, T. (1963). *The adiabatic motion of charged particles*. Interscience Publishers, New York.

[Øieroset et al., 2003] Øieroset, M., Phan, T. D., Fujimoto, M., , Chan, L., Lin, R. P., and Skoug, R. (2003). Spartial and temporal variations of the cold dense plasma sheet: Evidence for a low-lattitude boundary layer source? In Newell, P. T. and Onsager, T., editors, *Earth's Low-Latitude Boundary Layer, Geophys. Monogr. Ser.*, volume 133, page 253. AGU, Washtington. D. C.

[Park, 1958] Park, E. N. (1958). Dynamics of the interplanetary gas and magnetic fields. *Astrophys. J.*, 128:664.

[Peroomian, 2003] Peroomian, V. (2003). The influence of the interplanetary magnetic field on the entry of solar wind ions into the magnetosphere. *Geophys. Res. Lett.*, 30(1):doi:10.1029/2002GL016627.

[Petrinec and Russell, 1996] Petrinec, S. M. and Russell, C. T. (1996). Near-earth magnetotail shape and size as determined from the magnetopause flaring angle. *J. Geophys. Res.*, 101:137.

[Powell et al., 1999] Powell, K. G., Roe, . L., Linde, T. J., Gombosi, T. I., and DeZeeuw, K. L. (1999). A solution-adaptive upwind scheme for ideal magnetohydrodynamics. *J. Comput. Phys.*, 154:154.

[Raeder and et al., 1997] Raeder, J. and et al. (1997). Boundary layer formation in the magnetotail: Geotail observations and comparisons with a global MHD simulation. *Geophys. Res. Lett.*, 24(8):951.

[Richard et al., 2002] Richard, L., R., El-Alaoui, M., Ashour-Abdalla, M., and Walker, R. J. (2002). Interplanetary magnetic field control of the entry of solar energetic particles into the magnetosphere. *J. Geophys. Res.*, 107(A8):doi:10.1029/2001JA000099.

[Richard et al., 1994] Richard, L., R., Walker, R. J., and Ashour-Abdalla, M. (1994). The population of the magnetosphere by solar winds ions when the interplanetary magnetic field is northward. *Geophys. Res. Lett.*, 21(23):2455.

[Sckopke and et al., 1981] Sckopke and et al. (1981). Structure of the low-latitude boundary layer. *J. Geophys. Res.*, 86:2099.

[Song et al., 1999] Song, P., DeZeeuw, D. L., Gombosi, T. I., Groth, C. P. T., and Powell, K. G. (1999). A numerical study of solar windcmagnetosphere interaction for northward interplanetary magnetic field. *J. Geophys. Res.*, 104(A12):28361.

[Song et al., 1994] Song, P., Holzer, T., Russell, C. T., and Wang, Z. (1994). Modeling the low latitude boundary layer with reconnection entry. *Geophys. Res. Lett.*, 21:625.

[Terasawa and et al., 1997] Terasawa, T. and et al. (1997). Solar wind control of density and temperature in the near-earth plasma sheet:WIND/GEOTAIL collaboration. *Geophys. Res. Lett.*, 24:935.

[Vasyliunas, 1968] Vasyliunas, D. J. (1968). A survey of low energy electrons in the evening sector of the magnetosphere with OGO 1 and OGO 3. *J. Geophys. Res.*, 73:2839.

[Walker et al., 1976] Walker, J., R., Erickson, K. N., Swanson, R. L., and Winckler, J. R. (1976). Substorm-associated particle boundary motion at synchronous orbit. *J. Geophys. Res.*, 81:5541.

[Walker et al., 1996] Walker, J., R., Richard, R. L., Ogino, T., and Ashour-Abdalla, M. (1996). The population of the magnetosphere by solar winds ions when the interplanetary magnetic field is northward. *Physics of Space Plasmas*, page 561.

[Walt, 1994] Walt, M. (1994). *Introduction to geomagnetically trapped radiation*. Cambridge University Press.

[Watanabe et al., 2005] Watanabe, M., Kabin, K., Sofko, G. J., Rankin, R., Gombosi, T. I., Ridley, A. J., and Clauer, C. R. (2005). Internal reconnection for northward interplanetary magnetic field. *J. Geophys. Res.*, 110(A06210):doi:10.1029/2004JA010832.

[Wing and Newell, 2002] Wing, S. and Newell, P. T. (2002). 2D plasma sheet ion density and temperature profiles for northward and southward IMF. *Geophys. Res. Lett.*, 29(9):1307,doi:10.1029/2001GL013950.